AAS 18-448

AUTONOMOUS SWARMING FOR SIMULTANEOUS NAVIGATION AND ASTEROID CHARACTERIZATION

Nathan Stacey[*], **Simone D'Amico**[†]

Completed asteroid missions have utilized a single spacecraft and depended extensively on ground-based systems for radiometric measurements, data analysis, and computation of estimation algorithms. In contrast, this paper describes an autonomous mission and estimation architecture to simultaneously navigate and estimate an asteroid's attitude, gravity field, and shape online. A swarm composed of a single main spacecraft and multiple nanosatellites in closed orbits about an asteroid take inter-satellite radiometric measurements while cooperatively tracking asteroid landmarks with optical sensors. This fully controllable swarm offers stereovision capabilities and a more geometrically diverse measurement set than a single, monolithic spacecraft. Measurements are also available for a longer period of time than autonomous asteroid characterization mission concepts in literature that use passive probes, which lack orbit control capabilities. All swarm measurements are combined in a novel unscented Kalman filter. The filter computation time is significantly reduced with no loss of accuracy by exploiting the matrix square root triangular structure and employing modified equinoctial elements for efficient numerical integration. High fidelity simulation is used to demonstrate the achievable navigation and asteroid characterization accuracy of the proposed mission and estimation concept.

INTRODUCTION

Asteroids have become a major focus of the space community.[1] They offer a wealth of scientific knowledge including insights into how the solar system was formed,[1–3] and they contain valuable resources that could allow mining and in-situ resource utilization.[4] There is great interest in asteroids for planetary defense, especially considering the 2013 meteor explosion in Chelyabinsk, Russia. Additionally, NASA has identified a manned asteroid mission as a key technology enabler for a manned mission to Mars.[4]

Regardless of an asteroid mission's objective, it is vital that mission designers and scientists have key information such as the asteroid's orbit, rotational motion, shape, and gravity field. This information enables safe guidance, navigation, and control in proximity to asteroids and aids in selecting landing sites. The asteroid gravity field and shape also provide insight into the density distribution. Coarse information can be derived from a variety of sources including ground-based radar and telescopes as well as space-based telescopes. However, more detailed information is only available through measurements taken in proximity to the asteroid. In practice, asteroid missions have used ground-based radiometric measurements as well as optical navigation (OpNav) where the asteroid is tracked as a point at far range and individual features on the asteroid surface are tracked at close range.[5–8]

With the exception of Hayabusa 2,[9] every asteroid mission has utilized a single, monolithic spacecraft which is generally operated in either an orbiter or a flyby configuration. In an orbiter mission, the spacecraft approaches the asteroid and typically enters a high altitude survey orbit where a coarse shape model is constructed, the asteroid rotational motion is characterized, and low degree gravity coefficients are estimated. The effects of gravity are more observable closer to the asteroid center of mass (COM); however,

[*] Doctoral Candidate, Stanford University, Department of Aeronautics and Astronautics, Space Rendezvous Laboratory, Durand Building, 496 Lomita Mall, Stanford, CA 94305-4035

[†] Assistant Professor, Stanford University, Department of Aeronautics and Astronautics, Space Rendezvous Laboratory, Durand Building, 496 Lomita Mall, Stanford, CA 94305-4035

flying closer to the asteroid increases the risk of collision. Consequently, the spacecraft progressively moves to lower altitude orbits as the asteroid shape and gravity field are estimated with greater accuracy.[10,11]

Flyby missions where the spacecraft passes the target body in a hyperbolic orbit are attractive because they can be added as secondary objectives to other missions.[12] A good example is the NEAR spacecraft which flew by 253 Mathilde before continuing on to orbit 433 Eros.[13] Only coarse shape and gravity information are obtained from flybys because the mission duration is short. However, the short duration makes flyby missions inexpensive. Ground-based tracking and data analysis are required for a relatively short time, and little fuel is required when compared to an orbiter mission that requires station-keeping and orbit reconfiguration maneuvers for an extended period of time.

Every asteroid characterization mission to date has suffered from the same limitation: they depend extensively on ground-based systems for radiometric measurements and data processing as well as navigation, shape, and gravity estimation solutions.[10,14] Completed missions have required hours of daily tracking and communication with highly oversubscribed ground-based systems such as NASA's Deep Space Network (DSN).[14] Measurements tend to be processed by ground-based systems because batch estimation techniques are used,[10,14] which require too much memory and computational effort for onboard implementation. Mission designers must take into account that ground-based measurements and communication are not possible when the spacecraft is occulted from the Earth or when the DSN is not available. As a result of gaps in communication with the Earth and light time delay, the spacecraft must wait long periods of time before receiving navigation, shape, and gravity estimation solutions. Consequently, the spacecraft is slow to react to new measurements.

Authors have attempted to enable onboard estimation through sequential filters, which require less memory and computational effort than batch estimators. Most authors have turned to the extended Kalman filter (EKF)[15–18] which linearizes the dynamics and measurement models with the computation of often complex Jacobian matrices. Authors have also tried to minimize the need for ground-based measurements through the addition of inter-spacecraft measurements. Leonard et al.[15] found that two spacecraft orbiting an asteroid with a highly asymmetrical gravity field can simultaneously estimate the spacecraft states and the asteroid gravity coefficients using only relative radiometric measurements between the two satellites. The addition of ground-based measurements was found to greatly increase the accuracy of the estimated spacecraft states and minimally improve gravity recovery. Hesar et al.[16] found that augmenting Leonard et al.'s approach with OpNav significantly increases the estimation accuracy of the spacecraft states and gravity field. Atchison et al.[12,19,20] proposed a mission concept where a spacecraft in a hyperbolic orbit about an asteroid releases multiple probes into hyperbolic orbits that pass close to the asteroid. The spacecraft tracks the probes while the DSN radiometrically tracks the spacecraft. Although this mission concept enables the spacecraft to visit multiple asteroids, only μ and occasionally J_2 can be estimated because of the high velocity of the spacecraft relative to the asteroid and because measurements to the probes are available for a short time.[19] Fujimoto et al.[17] suggested placing two spacecraft in closed orbits about an asteroid. The two spacecraft take relative range measurements while optically tracking multiple probes in hyperbolic orbits about the asteroid. A benefit of the concepts proposed by Atchison et al. and Fujimoto et al. is that the main satellites remain a safe

Table 1: Summary of relevant multiple spacecraft asteroid characterization missions in literature.

	Author (Year)	DSN	OpNav	Inter-Satellite Measurements	Satellite State Representation	Satellite Orbits	Gravity Recovery	Estimation Technique
Two S/C	Leonard[15] (2012)	No	No	Range, Doppler	Cartesian	Orbiters	*DO 6	†EKF
	Hesar[16] (2015)	No	Yes	Range, Doppler	Cartesian	Orbiters	*DO 9	EKF
Swarm	Atchison[12,19,20] (2015, 2017)	Yes	No	Range, Doppler, Angles	Cartesian	Flybys	μ, (J_2)	Batch, EKF, UKF
	Fujimoto[17] (2016)	No	No	Range, Angles, Angle Rates	Cartesian	Orbiters & Flybys	*DO 5	EKF

*Degree and order.
†Uses the square-root information filter form of the EKF with measurement iteration.

distance from the asteroid while only the expendable probes pass close to the asteroid surface where gravitational effects are more observable and the risk of collisions is greater.

The mission architectures explored by these authors are summarized in Table 1. Each author uses a Cartesian satellite state representation and is able to estimate a different degree and order gravity field using simulated data. The mission concept of Hesar et al.[16] provides the most accurate spacecraft state and gravity coefficient estimation because it uses both inter-satellite radiometric measurements and landmark tracking. However, it is important to note that Hesar et al. and Fujimoto et al. only found lower bounds on the gravity recovery accuracy their proposed concepts could achieve for a simulated mission. The estimation algorithms were always linearized about the true state, which eliminated the possibility of divergence.[16,17,21] Also note that none of the papers listed in Table 1 included asteroid rotational motion parameters, sensor biases, or asteroid landmark positions in the estimated state.

This paper introduces the innovative Autonomous Nanosatellite Swarming (ANS) Using Radio-Frequency and Optical Navigation project, which is supported by the NASA Small Spacecraft Technology Program.[22] ANS is under development at Stanford University's Space Rendezvous Laboratory (SLAB) and comprises a set of novel dynamics, guidance, navigation, and control algorithms. This paper focuses on the ANS mission and estimation architectures, which provide improved autonomous navigation and concurrent asteroid characterization through a distributed spacecraft swarm. In contrast to passive probes which eventually collide with the asteroid or escape its gravity, the entire swarm is controllable and can be reconfigured. This provides a long term, geometrically diverse set of measurements. The swarm takes inter-spacecraft radio-frequency (RF) measurements and every spacecraft optically tracks asteroid landmarks, which has not been previously considered for asteroid gravity recovery. Measurements are processed in a novel unscented Kalman filter (UKF) that exploits the matrix square root triangular structure and utilizes modified equinoctial elements (MEE) for more efficient computation with no loss of accuracy. By limiting the use of ground-based systems, this architecture has the potential to reduce mission costs, enable a greater number of concurrent asteroid missions, and achieve more accurate characterization through autonomy.

The following section outlines the proposed mission concept along with key assumptions of the target asteroid. The next section presents a novel estimation architecture including the estimated state vector, dynamics and measurement models, and methodology for exploiting triangular structure (ETS) in the matrix square root in the UKF. Several case studies demonstrating the performance of the proposed mission and estimation concept are described in the subsequent section. Lastly, conclusions and concluding remarks are presented.

MISSION ARCHITECTURE

The current mission concept is compatible with the majority of asteroids in the solar system greater than 1 km in diameter. It would be extremely difficult to achieve bounded orbits about smaller targets for any appreciable amount of time without station-keeping maneuvers due to their weak gravity fields. To reduce complexity, it is assumed the target body is a single asteroid, which encompasses most asteroids including 85% of near-Earth asteroids.[13] Additionally, the target body is assumed to uniformly rotate about its maximum moment of inertia principal axis, which also comprises the majority of asteroids. Asteroids tend to enter this spin state as their energy dissipates over time because it is the minimum energy rotational state for a fixed magnitude of angular momentum.[23,24] The proposed mission can be broken into three phases. The first phase requires the aid of ground-based systems, while the second and third phases are completed autonomously.

Phase 1. Like a typical orbiter mission, the main spacecraft approaches the asteroid and first enters a high altitude survey orbit where ground assets aid in constructing a coarse shape model as well as estimating the asteroid rotational motion, gravitational parameter, and low degree gravity coefficients. The gravity coefficients may be estimated using the coarse shape model and an assumed uniform asteroid density.[23] The onboard shape model includes the estimated body-fixed Cartesian coordinates of points on the surface of the asteroid referred to as landmarks. For example, the landmarks could be the control points of stereo photoclinometry maplets or the center points of prominent craters.[5,6,25] A set of landmarks is selected for OpNav.

Phase 2. The main spacecraft releases multiple nanosatellites into bounded, safe orbits using a collision avoidance technique such as e/i vector separation.[26,27] The spacecraft take inter-satellite RF measurements while cooperatively tracking OpNav landmarks using optical sensors. A UKF is used to estimate the spacecraft states as well as the asteroid gravity field, rotational motion, and OpNav landmark body-fixed positions online. UKF computations and data processing are distributed amongst the swarm. However, only the main spacecraft has a high enough gain antenna to communicate with the Earth when necessary.

Phase 3. The fully controllable satellite swarm is reconfigured online for improved gravity recovery and shape estimation throughout the life of the mission. This approach offers a longer term, more geometrically diverse set of measurements than mission concepts employing passive probes.[17,19] Since the gravity field is more observable close to the asteroid, the swarm progressively moves to lower altitude orbits as the asteroid is characterized with greater accuracy. The autonomous swarm can safely enter lower altitude orbits than a traditional ground system dependent mission because navigation solutions and control inputs are computed online.

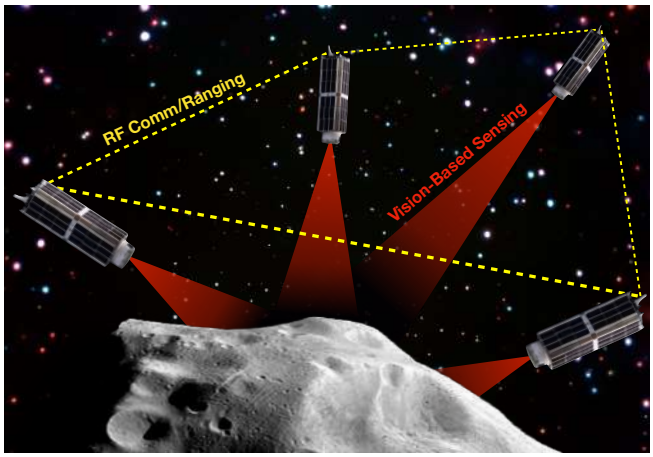

Figure 1: ANS mission concept for autonomous asteroid characterization using a satellite swarm.

ESTIMATION ARCHITECTURE

The goal of the estimation architecture it to provide robust, accurate, and computationally efficient estimation for online navigation and concurrent asteroid characterization. Table 2 describes the coordinate frames used in the algorithm and throughout this paper. The following paragraph substantiates the choice of estimation algorithm. This is followed by a discussion on the chosen state vector, dynamics models, and

Table 2: Definitions of coordinate frames used in this paper.

Asteroid Centered Inertial (ACI)	x-axis aligned with vernal equinox* y-axis completes right handed triad z-axis perpendicular to Earth mean-equatorial plane*
Asteroid Centered Asteroid Fixed (ACAF)	x-axis aligned with asteroid prime meridian† y-axis completes right handed triad z-axis aligned with mean spin axis
Camera Frame (CF)	x-axis parallel to image plane pixel columns y-axis parallel to image plane pixel rows z-axis aligned with camera boresight
Radial Transverse Normal (RTN)	R-axis aligned with vector from asteroid COM to spacecraft T-axis completes right-handed triad N-axis aligned with spacecraft angular momentum vector

*Defined at J2000 epoch.
†Defined with respect to prominent asteroid landmark.

measurement models. Then the new exploiting triangular structure (ETS) technique is delineated along with the ETS-UKF algorithm.

The UKF[28] effectively balances accuracy and computational effort for this mission concept. Particle filters and batch estimators require too much computational effort for onboard implementation considering satellite processors in the near future.[29,30] Additionally, the UKF is more accurate than the EKF for nonlinear systems. The UKF is also more robust to initial state estimate errors than the EKF and does not require computing Jacobian matrices, which are complex due to high degree gravity potential coefficients. In practice, the traditional UKF takes longer to run than the EKF. However, this paper presents a novel UKF algorithm that runs significantly faster than the traditional UKF with no loss of accuracy.

State Vector

The filter state is given by

$$\boldsymbol{x} = [\boldsymbol{MEE}_{\boldsymbol{1}}^T \ \ldots \ \boldsymbol{MEE}_{\boldsymbol{\kappa}}^T \, C_{R1} \ \ldots \ C_{R\kappa} \, \boldsymbol{\beta}^T \, \mu \, \boldsymbol{G}^T \, \alpha \, \delta \, W_0 \, w \, r_{pm} \, \phi_{pm} \, \boldsymbol{L}_{\boldsymbol{1}}^T \ \ldots \ \boldsymbol{L}_{\boldsymbol{\ell}}^T]^T \tag{1}$$

The definition of each parameter in Eq. (1) is provided in Table 3. The subscript κ is the number of spacecraft, and ℓ is the number of estimated OpNav landmark positions not including the landmark with respect to which the prime meridian is defined.

Table 3: State variable definitions.

Variable	Definition
$\boldsymbol{MEE}_{\boldsymbol{\kappa}}$	Osculating MEE of the κth spacecraft in the ACI frame
$C_{R\kappa}$	Radiation pressure coefficient of the κth spacecraft
$\boldsymbol{\beta}$	Vector containing estimated sensor biases
μ	Asteroid gravitational parameter
$\boldsymbol{G}$	Vector containing normalized gravity coefficients
α, δ, W_0	Angles describing asteroid attitude (See Archinal et al.[31])
w	Asteroid rotation rate
r_{pm}, ϕ_{pm}	Radius and latitude of prime meridian reference landmark
$\boldsymbol{L}_{\boldsymbol{\ell}}$	Cartesian position of ℓth OpNav landmark in the ACAF frame

To increase computational efficiency with the goal of onboard implementation, the spacecraft states are represented with MEE instead of the common Cartesian representation. The MEE are defined as[32]

$$\boldsymbol{MEE} = \begin{bmatrix} p \\ f \\ g \\ h \\ k \\ l \end{bmatrix} = \begin{bmatrix} a(1-e^2) \\ e\cos(\omega + f_r\Omega) \\ e\sin(\omega + f_r\Omega) \\ \tan^{f_r}(\frac{i}{2})\cos(\Omega) \\ \tan^{f_r}(\frac{i}{2})\sin(\Omega) \\ \nu + \omega + f_r\Omega \end{bmatrix} \tag{2}$$

where a, e, i, w, Ω, and ν are the classical Keplerian orbital elements and f_r is a constant that can be chosen as either positive or negative one. Typically, orbital element states such as MEE are numerically integrated more efficiently than Cartesian coordinates because only one variable changes rapidly whereas all six Cartesian variables change rapidly.[33] Additionally, an orbital element state can improve observability by decoupling observable and non-observable parameters as was found for angles only navigation in formation-flying and rendezvous.[34] However, orbital element states suffer from singularities that can limit their application. MEE are chosen because they have only one singularity at either $i = 180°$ when $f_r = 1$ or at $i = 0°$ when $f_r = -1$. Approaching the singularity leads to poor numerical integration of the MEE, but the singularity is easily avoided by either redefining the associated Cartesian frame or appropriately selecting the value of f_r.[35] For this paper, $f_r = 1$.

The asteroid gravity potential is represented with a spherical harmonic expansion expressed as[36]

$$U = \frac{GM}{r} \sum_{n=0}^{\infty} \sum_{m=0}^{n} \frac{R_{ref}}{r^n} \bar{P}_{nm}(\sin\phi)(\bar{C}_{nm}\cos(m\lambda) + \bar{S}_{nm}\sin(m\lambda)) \tag{3}$$

Here, G is the universal gravitational constant, r is the distance between the spacecraft and asteroid COM, $\bar{C}_{nm}$ and $\bar{S}_{nm}$ are the normalized spherical harmonic gravity potential coefficients of degree n and order m, and $\bar{P}_{nm}$ denotes the normalized associated Legendre functions. The gravity coefficient and associated Legendre function normalizations are defined by Vallado.[36] The reference mass and distance used to nondimensionalize the gravity coefficients are given by M and R_{ref} respectively.[36] These parameters are typically chosen as the asteroid mass and average radius. The variables ϕ and λ are the spacecraft latitude and longitude respectively in the ACAF frame. A drawback of the spherical harmonic gravity model is that it diverges within the Brillouin sphere, which is the smallest sphere that contains the entire body.[3] Nevertheless, the spherical harmonic gravity field is employed here because it is less computationally demanding than alternatives such as the mascon and polyhedron models which converge everywhere outside the body.[3,37] Additionally, the polyhedron model accuracy is limited by the accuracy of the asteroid shape model, and the mascon model has significant force computation errors even when large numbers of mascons are used.[37]

It is assumed that a fixed set of landmarks has already been selected for OpNav and that there exist coarse estimates of the body-fixed location of each OpNav landmark. The body-fixed coordinates of each of these OpNav landmarks are always included in the filter state and are denoted by $\boldsymbol{L_1} \dots \boldsymbol{L_\ell}$. The asteroid prime meridian is defined with respect to the center of a prominent landmark that is assigned a fixed longitude.[31] Consequently, only the distance from the asteroid COM, r_{pm}, and latitude, ϕ_{pm}, of the prime meridian reference landmark are estimated. This implicitly retains the location of the asteroid prime meridian throughout the mission.

Filter Dynamics Models

In the filter time update, the osculating MEE of each spacecraft are numerically integrated using the Gauss Variational Equations (GVE) formulated as[32,38]

$$\begin{bmatrix} \dot{p} \\ \dot{f} \\ \dot{g} \\ \dot{h} \\ \dot{k} \\ \dot{l} \end{bmatrix} = \begin{bmatrix} 0 & A & 0 \\ B & C & D \\ E & F & G \\ 0 & 0 & H \\ 0 & 0 & I \\ 0 & 0 & J \end{bmatrix} {}^{RTN}\boldsymbol{f} + \begin{bmatrix} 0 \\ 0 \\ 0 \\ 0 \\ 0 \\ K \end{bmatrix} \tag{4}$$

$$A = \frac{2}{W}\sqrt{\frac{p^3}{\mu}} \qquad B = \sin l\sqrt{\frac{p}{\mu}} \qquad C = \frac{f + (1+W)\cos l}{W}\sqrt{\frac{p}{\mu}}$$

$$D = \frac{g(k\cos l - h\sin l)}{W}\sqrt{\frac{p}{\mu}} \qquad E = -\cos l\sqrt{\frac{p}{\mu}} \qquad F = \frac{g + (1+W)\sin l}{W}\sqrt{\frac{p}{\mu}}$$

$$G = \frac{f(h\sin l - k\cos l)}{W}\sqrt{\frac{p}{\mu}} \qquad H = \frac{(1+h^2+k^2)\cos l}{2W}\sqrt{\frac{p}{\mu}} \qquad I = \frac{(1+h^2+k^2)\sin l}{2W}\sqrt{\frac{p}{\mu}}$$

$$J = \frac{h\sin l - k\cos l}{W}\sqrt{\frac{p}{\mu}} \qquad K = W^2\sqrt{\frac{\mu}{p^3}} \qquad W = 1 + f\cos l + g\sin l$$

where f_r has been selected as positive one. Here, ${}^{RTN}\boldsymbol{f}$ is the total perturbing acceleration experienced by the spacecraft expressed in the RTN frame, which is modeled as

$${}^{RTN}\boldsymbol{f} = \underset{ACI\to RTN}{\mathbf{R}} \left({}^{ACI}\boldsymbol{f}_{SRP} + {}^{ACI}\boldsymbol{f}_{3rd\ Body} + \underset{ACAF\to ACI}{\mathbf{R}} {}^{ACAF}\boldsymbol{f}_G \right) \tag{5}$$

The vectors $\boldsymbol{f}_{SRP}$, $\boldsymbol{f}_{3rd\ Body}$, and $\boldsymbol{f}_G$ are the accelerations due to solar radiation pressure (SRP), third body effects, and nonspherical gravity respectively. The superscript on the left of each vector indicates the frame in which the vector is expressed. Note that $\boldsymbol{f}_G$ is calculated in the ACAF frame and then expressed in the ACI frame using the rotation matrix ${}_{ACAF\rightarrow ACI}\mathbf{R}$ before it is summed with the other perturbing accelerations. The sum of the perturbing accelerations is then expressed in the spacecraft RTN frame using the rotation matrix ${}_{ACI\rightarrow RTN}\mathbf{R}$. The matrix ${}_{ACI\rightarrow RTN}\mathbf{R}$ is a function of the estimated spacecraft MEE, and ${}_{ACAF\rightarrow ACI}\mathbf{R}$ is a function of the estimated asteroid attitude. SRP induced accelerations can be modeled as[39]

$$\boldsymbol{f}_{SRP} = -P_{\odot} C_R \left(\frac{A}{m}\right) \frac{\boldsymbol{r}_S}{r_S} \tag{6}$$

where $P_{\odot}$ is the solar radiation pressure, A is the spacecraft cross-sectional area, m is the spacecraft mass, and $\boldsymbol{r}_S$ is the vector from the sun to the spacecraft COM. The solar radiation pressure is defined as[39]

$$P_{\odot} = \frac{\phi}{c} \tag{7}$$

where ϕ is the solar flux. The solar flux can be modeled by[23]

$$\phi = \frac{P_0}{R^2} \tag{8}$$

where P_0 is a solar constant approximately equal to 1x10$^8 \frac{\text{kg km}^3}{\text{s}^2\text{m}^2}$ and R is the distance from the sun.

During each filter time update, the MEE are numerically integrated in time using the fourth order Runge-Kutta method. Estimated sensor biases, asteroid rotational motion parameters, and estimated landmark positions expressed in the ACAF frame are modeled as constants. Therefore, the only state parameters that change when passed through the filter dynamics models are the osculating MEE.

Filter Measurement Models

In the current implementation, the swarm takes inter-spacecraft one way RF pseudo-range and doppler measurements as well as optical measurements to visible OpNav landmarks. The measurement models require the inertial Cartesian position, $\boldsymbol{r}$, and velocity, $\dot{\boldsymbol{r}}$, of each spacecraft COM relative to the asteroid COM, which is computed from the estimated spacecraft osculating MEE using the mapping provided by Broucke.[40] RF pseudo-range measurements are given by

$$\rho_{PR} = \rho + c(\delta t_2 - \delta t_1) + b \tag{9}$$
$$= \rho + c\Delta\delta t + b \tag{10}$$

where ρ is the geometric range between the the two spacecraft antennas, c is the speed of light, δt is the spacecraft clock offset from the true time, $\Delta\delta t$ is the difference in clock offsets between the receiving and transmitting spacecraft, and b is the sensor bias. The filter is not provided information to distinguish between the influence of sensor bias and a difference in clock offsets on pseudo-range measurements. Consequently, these two parameters are combined into a single bias, and the modeled pseudo-range measurement becomes

$$\rho_{PR} = \rho + b_{PR} \tag{11}$$

The geometric range is given by[39]

$$\rho = \|\boldsymbol{\rho}\| \tag{12}$$
$$= c\tau \tag{13}$$

where τ is the time from the first spacecraft signal transmission at time $(t-\tau)$ to the second spacecraft signal reception at time t. The vector, $\boldsymbol{\rho}$, points from the first spacecraft antenna to the second spacecraft antenna and is given by

$$\boldsymbol{\rho} = \boldsymbol{r}_2(t) + \boldsymbol{r}_{a2}(t) - \boldsymbol{r}_1(t-\tau) - \boldsymbol{r}_{a1}(t-\tau) \tag{14}$$

where $\boldsymbol{r}_a$ points from the spacecraft COM to its RF antenna, and the subscripts 1 and 2 refer to the transmitting and receiving spacecraft respectively. The vector $\boldsymbol{r}_a$ is computed using the known spacecraft geometry and the spacecraft attitude provided by an onboard star tracker. The value of ρ can be solved by assuming an initial value of τ and iterating on Eqs. (12) and (13).[39,41] The number of required iterations depends on the spacecraft relative separation and velocity. If the relative separation and velocity are small enough that $\boldsymbol{r}_1(t-\tau) \approx \boldsymbol{r}_1(t)$ and $\boldsymbol{r}_{a1}(t-\tau) \approx \boldsymbol{r}_{a1}(t)$, it may be sufficient to set $\tau = 0$ and solve Eq. (12).

The model for doppler shift range rate measurements is found by taking the time derivative of Eq. (12). Assuming the effects of spacecraft rotation are negligible, the range rate measurement is modeled by

$$\dot{\rho} = (\dot{\boldsymbol{r}}_2(t) - \dot{\boldsymbol{r}}_1(t-\tau)) \cdot \frac{\boldsymbol{\rho}}{\rho} + b_D \tag{15}$$

where b_D is the doppler sensor bias. Note that τ was found while computing the geometric range.

The expected pixel measurements from each spacecraft to each visible OpNav landmark are given by

$$\begin{bmatrix} u \\ v \end{bmatrix} = \frac{1}{w'} \begin{bmatrix} u' \\ v' \end{bmatrix} \tag{16}$$

where u', v', and w' are intermediary quantities defined by

$$\begin{bmatrix} u' \\ v' \\ w' \end{bmatrix} = \hat{\mathbf{K}} \underset{ACI \to CF}{\mathbf{R}} \begin{bmatrix} \underset{ACAF \to ACI}{\mathbf{R}} & -\boldsymbol{r} \end{bmatrix} \begin{bmatrix} \boldsymbol{L} \\ 1 \end{bmatrix} \tag{17}$$

Here, $\boldsymbol{r}$ is the spacecraft Cartesian position expressed in the ACI frame, $\boldsymbol{L}$ is the OpNav landmark position expressed in the ACAF frame, and $\hat{\mathbf{K}}$ is the matrix of known camera intrinsic parameters defined by

$$\hat{\mathbf{K}} = \begin{bmatrix} f_x & 0 & c_x \\ 0 & f_y & c_y \\ 0 & 0 & 1 \end{bmatrix} \tag{18}$$

where f_x and f_y indicate the camera focal length divided by the pixel pitch in the pixel column and row directions respectively. The vector, $\boldsymbol{c} = [c_x \; c_y]^T$, denotes the principal point in units of pixels. In the filter measurement update, the expected optical measurements given by Eq. (16) are compared with the real optical measurements which have been undistorted using the known camera distortion coefficients. Measurements should be taken at a sufficient rate to capture the acceleration due to the highest frequency estimated gravity coefficient. The frequency of this coefficient is higher at lower altitudes, which requires a higher measurement rate. Note that each measurement type is a highly nonlinear function of the estimated state variables, which supports using a nonlinear filter like the UKF.

Exploiting Triangular Structure in the Matrix Square Root

In the UKF time update, sigma points are computed and then passed through the nonlinear filter dynamics models one at a time. Sigma points are computed again in the measurement update and passed through the nonlinear measurement models. In order to compute sigma points, the matrix square root of the covariance matrix, $\boldsymbol{\Sigma}$, must be calculated. Although there are many ways to compute the matrix square root, the most computationally efficient method uses Cholesky decomposition.[42] The Cholesky decomposition of $\boldsymbol{\Sigma}$ yields a lower triangular matrix, $\boldsymbol{\Gamma}$, that satisfies $\boldsymbol{\Gamma}\boldsymbol{\Gamma}^T = \boldsymbol{\Sigma}$. The sigma points are defined as[43]

$$\begin{aligned} \boldsymbol{\chi}_{[0]} &= \boldsymbol{\mu} \\ \boldsymbol{\chi}_{[i]} &= \boldsymbol{\mu} + \boldsymbol{A}_{[i]} && \text{for } i = 1, ..., n \\ \boldsymbol{\chi}_{[i]} &= \boldsymbol{\mu} - \boldsymbol{A}_{[i-n]} && \text{for } i = n+1, ..., 2n \end{aligned} \tag{19}$$

where $\boldsymbol{\chi}_{[i]}$ is the ith sigma point, $\mathbf{A} = \sqrt{n+\psi}\boldsymbol{\Gamma}$, n is the number of state variables, $\psi = \theta^2(n+\eta) - n$, and θ and η are scaling parameters that determine how far sigma points are sampled from the mean state estimate,

$\boldsymbol{\mu}$. Note that $\mathbf{A}$ is a lower triangular matrix, the subscript i indicates the ith column of $\mathbf{A}$, and each sigma point, $\boldsymbol{\mathcal{X}}_{[i]}$, is the ith column of the matrix $\boldsymbol{\mathcal{X}}$. If a sigma point is invalid because a spacecraft is within the Brillouin sphere, sigma points are recomputed after decreasing θ and η.

The traditional UKF quickly becomes computationally intensive as the number of spacecraft, degree and order of the estimated gravity field, and number of estimated landmark positions increase. Consider a mission with three spacecraft estimating a degree and order ten gravity field and the positions of 200 OpNav landmarks. The state vector contains $n \approx 750$ parameters which requires $3(2n+1) \approx 4,500$ orbit propagations at each filter call. Assuming 20% of the OpNav landmarks are visible, there are about 369,250 optical measurements at each filter call in addition to about 6,000 inter-spacecraft RF measurements. Orbit propagations require significant computational effort because they are computed through numerical integration considering a high degree and order gravity field. A large number of measurements can also be computationally expensive because they are nonlinear functions of the state variables.

The total traditional UKF run time can be divided into three groups: (1) propagating the state vector in the time update, (2) computing measurements in the measurement update, and (3) all other computations, which includes computing the matrix square root. For the proposed architecture, the only computation required to propagate the state vector is the numerical integration of the MEE. Figure 2 shows what fraction of the total filter run time is due to each of the three groups of computations when a traditional UKF is used. Clearly, propagating the state vector heavily dominates the UKF run time. Although measurements do not have a large impact on run time for this paper, they could have a more significant impact for other applications with more computationally intensive measurement models and less computationally intensive dynamics models. Literature on reducing computation time for UKF simultaneous localization and mapping tends to focus on reducing time spent computing the matrix square root, which can be a significant portion of the total filter run time for applications with simple dynamics and measurement models.[44,45] In contrast, the newly proposed ETS-UKF reduces computation time in propagating the state vector and computing measurements with no loss of accuracy through ETS in the matrix square root. Although this technique will be described in the context of swarm asteroid characterization, it is applicable to any UKF with partially decoupled state parameter dynamics or with any measurement that is not a function of every state parameter.

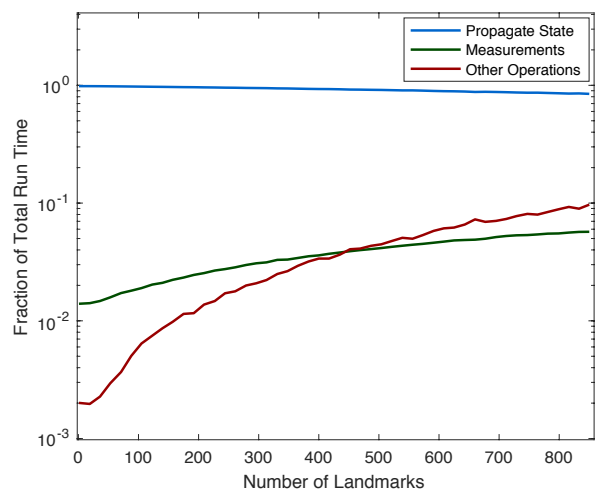

Figure 2: Percent of total traditional UKF run time required for each group of operations. This plot considers a mission with three spacecraft where measurements are available every five minutes. A 37.5 second numerical integration time step is used and 20% of the OpNav landmarks are visible.

Time Update. By appropriately ordering the state variables, orbit propagations from the zeroth sigma point can be reused for other sigma points. For this reason, the state variables are ordered in κ+2 groups as

$$\boldsymbol{x} = [\overset{1}{\mu\ \boldsymbol{G}^T\ \alpha\ \delta\ W_0\ w} \mid \overset{2}{\boldsymbol{MEE}_{\mathbf{1}}^T\ C_{R1}} \mid \ldots \mid \overset{\kappa+1}{\boldsymbol{MEE}_{\boldsymbol{\kappa}}^T\ C_{Rk}} \mid \overset{\kappa+2}{\boldsymbol{\beta}^T\ r_{pm}\ \phi_{pm}\ \boldsymbol{L}_{\mathbf{1}}^T\ \ldots\ \boldsymbol{L}_{\boldsymbol{\ell}}^T}]^T \tag{20}$$

The parameters in group 1 affect the dynamics of every spacecraft. Those in group 2 only affect the first spacecraft dynamics, and those in group κ+1 only affect the κth spacecraft dynamics. Those in group κ+2 do not affect any spacecraft dynamics.

Many sigma points have parameter values that match the mean because $\mathbf{A}$ is a lower triangular matrix. Sigma points whose group 1 and group 2 parameters match the mean can reuse the first spacecraft propagation from the zeroth sigma point. Sigma points whose group 1 through group 3 parameters match the mean can reuse the first and second spacecraft propagations from the zeroth sigma point. Sigma points that only differ from the mean in group κ+2 parameters can reuse every spacecraft propagation from the zeroth sigma point. This reduces the number of spacecraft propagations every time the filter is called and allows for a large number of landmark locations to be estimated with little additional computation time.

For the estimated state considered in this paper, the number of state variables is given by

$$n = g + a + 7\kappa + b + s + 3\ell + 1 \tag{21}$$

where g is the number of elements in $\boldsymbol{G}$, $a = 4$ is the number of estimated asteroid attitude parameters, κ is the number of spacecraft, b is the number of elements in $\boldsymbol{\beta}$, $s = 2$ accounts for the estimated prime meridian reference landmark spherical coordinates, ℓ is the number of estimated OpNav landmark positions, and the one accounts for μ. Therefore, the number of orbit propagations the traditional mechanization requires at every filter call is

$$\begin{aligned} \text{UKF Orbit Propagations} &= \kappa(2n+1) \\ &= 2\kappa(g + a + 1.5) + 14\kappa^2 + 2\kappa(b + s + 3\ell) \end{aligned} \tag{22}$$

Through ETS, the number of orbit propagations required each time the filter is called is reduced to

$$\text{ETS-UKF Orbit Propagations} = 2\kappa(g + a + 1.5) + 14\sum_{i=0}^{\kappa-1}(\kappa - i) \tag{23}$$

For a mission with five spacecraft estimating a degree and order eight gravity field as well as 300 landmark positions, ETS reduces the number of required orbit propagations from 10,285 to 1,045. This translates to about an order of magnitude reduction in computation time in the time update. It is important to note that the number of orbit propagations in the ETS-UKF does not depend on the number of estimated sensor parameters or landmark locations as can be seen in Eq. (23). A simple example of ETS in the time update is included in Appendix A.

Measurement Update. By appropriately reordering the state variables after the time update is complete, measurements from the zeroth sigma point can be reused for other sigma points. First, it is necessary to differentiate between visible and hidden landmarks. At each filter call, an OpNav landmark is considered visible if optical measurements of that OpNav landmark are available. In other words, that OpNav landmark was matched to a landmark in an image. Conversely, an OpNav landmark is considered hidden if no optical measurement of that OpNav landmark is available at that filter call. In this paper, it is assumed that there is always correct correspondence between observed landmarks and OpNav landmarks. In order to exploit the triangular structure of the matrix square root in the measurement update, the state variables are ordered in p+5 groups as

$$\boldsymbol{x} = [\overset{1}{\alpha\ \delta\ W_0\ w\ \boldsymbol{MEE_1^T} \ldots \boldsymbol{MEE_\kappa^T}}\big|\overset{2}{r_{pm}\ \phi_{pm}}\big|\overset{3}{{}^{\boldsymbol{v}}\boldsymbol{L_1^T}}\big|\ldots\big|\overset{p+2}{{}^{\boldsymbol{v}}\boldsymbol{L_p^T}}\big|\overset{p+3}{\boldsymbol{\beta_{PR}^T}}\big|\overset{p+4}{\boldsymbol{\beta_D^T}\ \mu}\big|\overset{p+5}{{}^{\boldsymbol{h}}\boldsymbol{L_1^T} \ldots {}^{\boldsymbol{h}}\boldsymbol{L_q^T}\ \boldsymbol{G^T}\ \boldsymbol{C_R}}]^T \tag{24}$$

where p is the number of OpNav landmarks that are visible to the swarm, and q is the number of OpNav landmarks that are hidden to the swarm. The superscripts, v and h, indicate landmarks that are visible and hidden to the swarm respectively. The vector $\boldsymbol{\beta}$ is separated into a vector containing the pseudo-range biases, $\boldsymbol{\beta_{PR}}$, and a vector containing the doppler biases, $\boldsymbol{\beta_D}$. The vector, $\boldsymbol{C_R}$, contains the radiation pressure coefficients of each spacecraft.

Sigma points that match the mean in group 1 and group 2 parameters can reuse the optical measurements from the zeroth sigma point for each spacecraft to the prime meridian reference landmark. Sigma points that match the mean in groups 1 through 3 can reuse the optical measurements from each spacecraft to the prime meridian reference landmark and first visible OpNav landmark. Every optical measurement from the zeroth sigma point can be reused for sigma points that match the mean in groups 1 through p+2. Sigma points that match the mean in groups 1 through p+3 can reuse every inter-spacecraft RF range measurement from the zeroth sigma point. Every inter-spacecraft RF doppler measurement from the zeroth sigma point can be reused for sigma points that match the mean in groups 1 through p+4. Note that μ affects the spacecraft velocity in the transformation from MEE to Cartesian coordinates, which in turn affects the doppler measurements.

In the traditional UKF, each of the $2n$+1 sigma points are passed through the measurement models. Therefore, the number of computed measurements during every filter call is

$$\begin{aligned}\text{UKF Optical Measurements} &= 2\kappa(p+1)(2n+1)\\ &= 4\kappa(p+1)(a+6\kappa+s+0.5)+12\kappa(p+1)p+4\kappa(p+1)(g+\kappa+b+3q+1)\end{aligned} \tag{25}$$

$$\begin{aligned}\text{UKF RF Measurements} &= 2(\kappa-1)(2n+1)\\ &= 4(\kappa-1)(a+6\kappa+s+3p+b_{pr}+0.5b_d+1)+4(\kappa-1)(g+\kappa+0.5b_d+3q+0.5)\end{aligned} \tag{26}$$

where b_{pr} and b_d are the number of elements in $\boldsymbol{\beta}_{PR}$ and $\boldsymbol{\beta}_D$ respectively. Through ETS, the number of measurement computations required each time the filter is called is reduced to

$$\text{ETS-UKF Optical Measurements} = 4\kappa(p+1)(a+6\kappa+s+0.5)+12\kappa\sum_{i=0}^{p-1}(p-i) \tag{27}$$

$$\text{ETS-UKF RF Measurements} = 4(\kappa-1)(a+6\kappa+s+3p+b_{pr}+0.5b_d+1) \tag{28}$$

In Eqs. (26) and (28) it is assumed that the main spacecraft takes range and doppler measurements to each nanosatellite and that no RF measurements are taken between nanosatellites. Consider a mission with four spacecraft estimating a degree and order 12 gravity field as well as 350 landmark positions where 10% of the OpNav landmarks are visible. ETS reduces the number of required optical measurement computations in the measurement update from 1,428,520 to 119,608 and the number of required RF measurements from 15,090 to 2,946. Note that simply omitting hidden landmarks from the estimated state at each filter call results in a loss of accuracy.[43] In contrast, ETS results in no loss of accuracy and yields a greater reduction of computation time than omitting hidden landmarks from the estimated state. Although the technique presented by Huang et al.[45] also reduces the number of dynamics and measurement model computations, ETS reduces these computations further for systems that have either multiple vehicles or multiple measurements at each filter call. A simple example of ETS in the measurement update is included in Appendix A.

ETS-UKF Algorithm

The ETS-UKF algorithm is described in Table 4. The algorithm requires seven inputs where $\boldsymbol{u}$ is the control input, $\boldsymbol{z}$ is the measurement vector, $\mathbf{Q}$ is the process noise, $\mathbf{R}$ is the measurement noise, and $\boldsymbol{\mathcal{P}}$ is a permutation matrix. The initial mean state estimate, $\boldsymbol{\mu}^{[t-1]}$, should be ordered for ETS in the time update as illustrated by Eq. (20). The permutation matrix is the only input not required by the traditional UKF. It is used to reorder the optimal state for ETS in the time update to the optimal state for ETS in the measurement update. The superscripts $[t]$ and $[t-1]$ indicate the time step.

Line 2 computes $2n+1$ sigma points from the estimated mean and formal covariance at time step $t-1$ using Eq. (19). In line 3, a traditional UKF would pass every sigma point through the filter dynamics models. However, the ETS-UKF reuses dynamics model computations from the zeroth sigma point for other sigma points, which is indicated by the breve symbol above $\boldsymbol{g}$. The predicted mean and covariance are calculated in

Table 4: The ETS-UKF algorithm.

1:	Algorithm ETS-UKF($\boldsymbol{\mu}^{[t-1]}, \boldsymbol{\Sigma}^{[t-1]}, \boldsymbol{u}^{[t]}, \boldsymbol{z}^{[t]}, \mathbf{Q}^{[t]}, \mathbf{R}^{[t]}, \boldsymbol{\mathcal{P}}^{[t]}$):
	Time Update
2:	$\boldsymbol{\mathcal{X}} = [\boldsymbol{\mu}^{[t-1]} \quad \boldsymbol{\mu}^{[t-1]} + \mathbf{A} \quad \boldsymbol{\mu}^{[t-1]} - \mathbf{A}]$
3:	$\bar{\boldsymbol{\mathcal{X}}}^* = \breve{\boldsymbol{g}}(\boldsymbol{u}^{[t]}, \boldsymbol{\mathcal{X}})$
4:	$\bar{\boldsymbol{\mu}} = \bar{\boldsymbol{\mathcal{X}}}^* \boldsymbol{w}_m$
5:	$\bar{\boldsymbol{\Sigma}} = \sum_{i=0}^{2n} w_{c,i}(\bar{\boldsymbol{\mathcal{X}}}_i^* - \bar{\boldsymbol{\mu}})(\bar{\boldsymbol{\mathcal{X}}}_i^* - \bar{\boldsymbol{\mu}})^T + \mathbf{Q}^{[t]}$
	Measurement Update
6:	$\bar{\boldsymbol{\mu}}^* = \boldsymbol{\mathcal{P}}\bar{\boldsymbol{\mu}}$
7:	$\bar{\boldsymbol{\Sigma}}^* = \boldsymbol{\mathcal{P}}\bar{\boldsymbol{\Sigma}}\boldsymbol{\mathcal{P}}^T$
8:	$\bar{\boldsymbol{\mathcal{X}}} = [\bar{\boldsymbol{\mu}}^* \quad \bar{\boldsymbol{\mu}}^* + \mathbf{A}^* \quad \bar{\boldsymbol{\mu}}^* - \mathbf{A}^*]$
9:	$\bar{\mathbf{Z}} = \breve{\boldsymbol{h}}(\bar{\boldsymbol{\mathcal{X}}})$
10:	$\hat{\boldsymbol{z}} = \bar{\mathbf{Z}}\boldsymbol{w}_m$
11:	$\mathbf{S} = \sum_{i=0}^{2n} w_{c,i}(\bar{\mathbf{Z}}_i - \hat{\boldsymbol{z}})(\bar{\mathbf{Z}}_i - \hat{\boldsymbol{z}})^T + \mathbf{R}^{[t]}$
12:	$\bar{\boldsymbol{\Sigma}}^{x,z} = \sum_{i=0}^{2n} w_{c,i}(\bar{\boldsymbol{\mathcal{X}}}_i - \bar{\boldsymbol{\mu}}^*)(\bar{\mathbf{Z}}_i - \hat{\boldsymbol{z}})^T$
13:	$\mathbf{K} = \bar{\boldsymbol{\Sigma}}^{x,z}\mathbf{S}^{-1}$
14:	$\boldsymbol{\mu}^{*[t]} = \bar{\boldsymbol{\mu}}^* + \mathbf{K}(\boldsymbol{z}^{[t]} - \hat{\boldsymbol{z}})$
15:	$\boldsymbol{\Sigma}^{*[t]} = \bar{\boldsymbol{\Sigma}}^* - \mathbf{KSK}^T$
16:	$\boldsymbol{\mu}^{[t]} = \boldsymbol{\mathcal{P}}^T\boldsymbol{\mu}^{*[t]}$
17:	$\boldsymbol{\Sigma}^{[t]} = \boldsymbol{\mathcal{P}}^T\boldsymbol{\Sigma}^{*[t]}\boldsymbol{\mathcal{P}}$
18:	return $\boldsymbol{\mu}^{[t]}, \boldsymbol{\Sigma}^{[t]}$

lines 4-5 using two weighting vectors, $\boldsymbol{w}_m$ and $\boldsymbol{w}_c$, defined as[43]

$$w_{m,0} = \frac{\psi}{n+\psi} \tag{29}$$

$$w_{c,0} = \frac{\psi}{n+\psi} + (1 - \theta^2 + \zeta) \tag{30}$$

$$w_{m,i} = w_{c,i} = \frac{1}{2(n+\psi)} \qquad \text{for } i = 1, ..., 2n \tag{31}$$

where the subscript i refers to the ith element of the vector. The parameter ζ can be used to encode higher order information about the underlying distribution. If the true underlying distribution is Gaussian, the optimal choice is $\zeta = 2$.[43] The permutation matrix is used in line 6 to reorder the optimal state for ETS in the time update to the optimal state for ETS in the measurement update. When reordering the state, the formal covariance must be transformed accordingly. The predicted formal covariance matrix is defined as

$$\bar{\boldsymbol{\Sigma}} = E[(\boldsymbol{x}^{[t]} - \bar{\boldsymbol{\mu}})(\boldsymbol{x}^{[t]} - \bar{\boldsymbol{\mu}})^T] \tag{32}$$

where $\boldsymbol{x}^{[t]}$ is the true state at time t. When the mean state estimate is multiplied by $\boldsymbol{\mathcal{P}}$ in line 6, the transformed predicted covariance matrix is defined as

$$\begin{aligned} \bar{\boldsymbol{\Sigma}}^* &= E[(\boldsymbol{\mathcal{P}}\boldsymbol{x}^{[t]} - \boldsymbol{\mathcal{P}}\bar{\boldsymbol{\mu}})(\boldsymbol{\mathcal{P}}\boldsymbol{x}^{[t]} - \boldsymbol{\mathcal{P}}\bar{\boldsymbol{\mu}})^T] \\ &= \boldsymbol{\mathcal{P}}E[(\boldsymbol{x}^{[t]} - \bar{\boldsymbol{\mu}})(\boldsymbol{x}^{[t]} - \bar{\boldsymbol{\mu}})^T]\boldsymbol{\mathcal{P}}^T \\ &= \boldsymbol{\mathcal{P}}\bar{\boldsymbol{\Sigma}}\boldsymbol{\mathcal{P}}^T \end{aligned} \tag{33}$$

as seen in line 7. Given $\bar{\mathbf{\Sigma}}$ is positive definite, it is clearly shown that $\bar{\mathbf{\Sigma}}^*$ is positive definite by

$$\begin{aligned} \hat{\boldsymbol{x}}^T \bar{\mathbf{\Sigma}}^* \hat{\boldsymbol{x}} &= \hat{\boldsymbol{x}}^T \boldsymbol{\mathcal{P}} \bar{\mathbf{\Sigma}} \boldsymbol{\mathcal{P}}^T \hat{\boldsymbol{x}} \\ &= (\boldsymbol{\mathcal{P}}^T \hat{\boldsymbol{x}})^T \bar{\mathbf{\Sigma}} (\boldsymbol{\mathcal{P}}^T \hat{\boldsymbol{x}}) \\ &> 0 \quad \forall \ \hat{\boldsymbol{x}} \neq \mathbf{0} \end{aligned} \tag{34}$$

The matrix, $\bar{\mathbf{\Sigma}}^*$, must be positive definite in order to use Cholesky decomposition in line 8 to compute sigma points for the measurement update. In line 8, $\mathbf{A}^* = \sqrt{n+\psi}\mathbf{\Gamma}^*$ and $\mathbf{\Gamma}^*$ comes from the Cholesky decomposition of $\bar{\mathbf{\Sigma}}^*$. In other words, $\mathbf{\Gamma}^*$ satisfies $\mathbf{\Gamma}^* \mathbf{\Gamma}^{*T} = \bar{\mathbf{\Sigma}}^*$. The expected measurements for each sigma point are calculated in line 9. Measurements from the zeroth sigma point are reused for other sigma points when possible as indicated by the breve symbol above $\boldsymbol{h}$. Lines 10 and 11 find the predicted measurement vector, $\hat{\boldsymbol{z}}$, and its uncertainty, $\mathbf{S}$. Line 12 computes the cross-covariance, $\bar{\mathbf{\Sigma}}^{x,z}$, between the state and measurement vector, which is used to find the Kalman gain, $\mathbf{K}$, in line 13. In lines 14-15, the Kalman gain is used to compute the updated mean state estimate, $\boldsymbol{\mu}^{*[t]}$, and formal covariance, $\mathbf{\Sigma}^{*[t]}$, according to the state vector ordering for ETS in the measurement update. Lines 16 and 17 transform the updated mean state estimate and formal covariance back to the original ordering for ETS in the time update. Following the same reasoning in Eq. (34), it is easily shown that the updated covariance matrix ordered for ETS in the time update, $\mathbf{\Sigma}^{[t]}$, is positive definite. It is important to note that the ETS-UKF algorithm is identical to the traditional UKF[43] except for lines 3, 6-7, 9, and 16-17.

The ETS-UKF is most effective in reducing computation time when the time required to propagate the state vector and compute measurements dominates total filter run time. In cases where either propagating the state vector or computing measurements is much more computationally intensive than the other, it may be sufficient to just use ETS in either the time or measurement update. If ETS is only used in either the time or measurement update, only one state ordering is needed and lines 6-7 and 16-17 in Table 4 can be omitted. For this paper, the full ETS-UKF algorithm is utilized.

CASE STUDIES

The purpose of the following case studies is to demonstrate 1) the benefits of multiple spacecraft tracking asteroid landmarks, 2) the achievable navigation, shape, and gravity estimation accuracy of the proposed architecture, and 3) the computational savings of the ETS-UKF. This is accomplished by comparing the performance of two mission architectures in two orbit scenarios both with and without filter initial state estimate error. The two mission architectures are summarized in Table 5. In the first mission architecture, referred to as monocular, only the main spacecraft optically tracks asteroid OpNav landmarks while taking RF measurements to a single nanosatellite. This is similar to the mission concept proposed by Hesar et al.[16] The second architecture, referred to as stereo, utilizes the mission concept proposed in this paper with three spacecraft where the main spacecraft takes RF measurements to each of the two nanosatellites and every spacecraft optically tracks OpNav landmarks. Both mission architectures use the ETS-UKF. The asteroid 433 Eros is used for each simulation because accurate shape and gravity models are available from the NEAR mission which ended in 2001.[10,46,47] In each simulation, a degree and order ten gravity field is estimated as well as the positions of the same set of 200 OpNav landmarks.

Table 5: Case study mission architecture descriptions.

Mission Architecture	Number of Spacecraft	Number of Spacecraft Tracking Landmarks	Inter-Spacecraft RF Links
Monocular	2	1	1
Stereo	3	3	2

Orbit Scenario Descriptions

50 km Orbit Scenario. Each spacecraft is placed in a 50 km mean semi-major axis orbit. It is assumed that the swarm is in the third mission phase where the satellites progressively move to lower altitude orbits as

the asteroid is characterized with greater accuracy. Consequently, coarse estimates of the state parameters are available from earlier in the mission. The a priori formal covariance matrix provided to the filter is composed of the variances of the state parameters corresponding to Table 6 where the uncertainties in spacecraft position and velocity are mapped to MEE space using the unscented transform.[43] The uncertainties listed in Table 6 are similar to typical initial uncertainties used by the NEAR mission batch estimator.[10] The simulation lasts for ten orbit periods, which is about 297 hours.

35 km Orbit Scenario. Each spacecraft is placed in a 35 km semi-major axis orbit. For each mission architecture, the initial true error and formal variance of each parameter is taken as the final true error and formal variance of that parameter for the 50 km orbit scenario. This simulates the swarm moving to the 35 km orbit scenario after completing the 50 km orbit scenario. The 35 km orbit scenario lasts for 20 orbit periods, which is about 355 hours.

Table 6: A priori formal 1-σ uncertainty provided to the filter for the 50 km orbit scenario. Percentages refer to percent of true value.

Parameter	A Priori Uncertainty	Parameter	A Priori Uncertainty
Spacecraft Position $[x, y, z]$	1 km	Spacecraft Velocity $[\dot{x}, \dot{y}, \dot{z}]$	1 mm/s
μ	5%	$[L_x, L_y, L_z]$	100 m
w	1%	r_{pm}	100 m
C_R	10%	$\phi_{pm}, \alpha, \delta, W_0$	0.1°
b_{PR}, b_D	10%	$\bar{C}_{nm}, \bar{S}_{nm}$	0.005

First, both orbit scenarios are simulated for each mission architecture where the initial state estimate provided to the filter in the 50 km orbit scenario is the true state. The orbit scenarios are then simulated a second time where the initial state estimate provided to the filter in the 50 km orbit scenario is randomly drawn from a multivariate Gaussian distribution. The mean and covariance of the distribution are the true initial state and initial formal covariance matrix provided to the filter respectively. For the case of a random initial state estimate in the 50 km orbit scenario, both mission architectures are provided with the same initial state estimate errors. In each orbit scenario, the main spacecraft and nanosatellite of the monocular architecture are given the same initial orbital elements as the main spacecraft and first nanosatellite of the stereo architecture.

The measurement rate for the case studies is chosen by considering a 35 km retrograde, equatorial orbit about Eros. For a degree and order ten gravity field, the acceleration due to the highest frequency gravity coefficient completes an oscillation every 24 min. Although the orbits in these case studies are not equatorial, 24 min is a reasonable approximation of the period of the highest frequency gravity coefficient. In order to accurately estimate the gravity field, measurements are taken every five minutes, and the filter dynamics model numerical integration uses a 37.5 second time step. Geometric range is calculated in the filter by setting τ equal to zero and solving Eq. (12). This is an appropriate approximation because $\boldsymbol{r}_1(t-\tau) \approx \boldsymbol{r}_1(t)$ and $\boldsymbol{r}_{a1}(t-\tau) \approx \boldsymbol{r}_{a1}(t)$.

Absolute and Relative Orbit Geometry

The satellites are placed in near-circular, retrograde orbits for stability,[23] and each spacecraft is given the same initial mean semi-major axis to prevent secular drift in the along-track direction. The specified initial mean elements of each satellite are transformed to osculating elements using the mapping provided by Schaub and Junkins, which considers the effects of J_2 only.[48] Collisions are avoided using e/i vector separation in selecting the initial mean spacecraft orbital elements.[26] E/i vector separation leverages the relative geometry information encapsulated in quasi-nonsingular relative orbital elements (ROE). The ROE are defined in terms of the classical Keplerian orbital elements as

$$\begin{bmatrix} \delta a \\ \delta \lambda \\ \delta e_x \\ \delta e_y \\ \delta i_x \\ \delta i_y \end{bmatrix} = \begin{bmatrix} (a_d - a_c)/a_c \\ u_d - u_c + (\Omega_d - \Omega_c)\cos(i_c) \\ e_d\cos(w_d) - e_c\cos(w_c) \\ e_d\sin(w_d) - e_c\sin(w_c) \\ i_d - i_c \\ (\Omega_d - \Omega_c)\sin(i_c) \end{bmatrix} \tag{35}$$

where $u = M + w$ is the mean argument of latitude and the subscripts c and d indicate the chief and deputy respectively. Here, the main spacecraft is treated as the chief and each nanosatellite is considered a deputy. The relative eccentricity vector is defined as $\boldsymbol{\delta e} = [\delta e_x \ \delta e_y]^T$ and the relative inclination vector is defined as $\boldsymbol{\delta i} = [\delta i_x \ \delta i_y]^T$. The magnitudes of the relative eccentricity and inclination vectors are denoted by δe and δi respectively.

For $\delta a = 0$, a circular chief orbit, and under two-body acceleration only, the maximum separation between the chief and deputy in the chief radial direction is $a_c\delta e$. The maximum separation in the chief cross track direction is $a_c\delta i$. When the relative eccentricity vector is parallel or anti-parallel to the relative inclination vector, the minimum cross track separation occurs at the point of maximum radial separation, and the minimum radial separation occurs at the point of maximum cross track separation. This guarantees the chief and deputy are always separated by at least $\min\{a_c\delta e, a_c\delta i\}$.[26] This technique can be extended to multiple spacecraft to ensure all spacecraft are separated by a specified minimum distance.[27]

Table 7: Initial mean main spacecraft MEE and nanosatellite ROE of each simulation defined with respect to the ACI frame. Each ROE is multiplied by the main spacecraft semi-major axis.

Main Spacecraft MEE		Nanosatellite 1 ROE [km]		Nanosatellite 2 ROE [km]	
p	49.995, 34.997 km	$a_c\delta a$	0	$a_c\delta a$	0
f	-7.66x10^{-4}	$a_c\delta\lambda$	-5	$a_c\delta\lambda$	-10
g	-6.43x10^{-4}	$a_c\delta e_x$	2	$a_c\delta e_x$	4
h	-0.643	$a_c\delta e_y$	0	$a_c\delta e_y$	0
k	-0.539	$a_c\delta i_x$	2	$a_c\delta i_x$	4
l	-52.9°	$a_c\delta i_y$	0	$a_c\delta i_y$	0

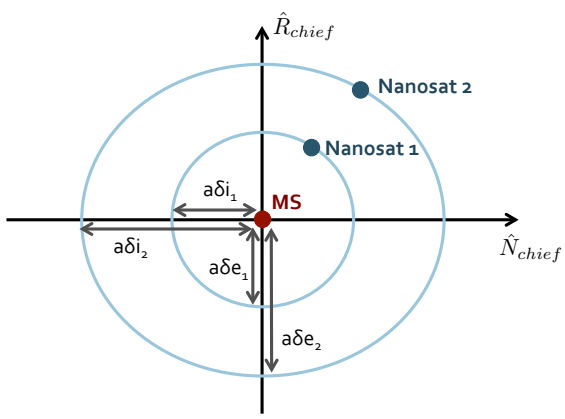

Figure 3: Motion of the nanosatellites with respect to the main spacecraft (MS) expressed in the main spacecraft RTN frame under the influence of asteroid two-body gravity only and for a circular chief orbit.

The initial nanosatellite mean ROE shown in Table 7 are chosen such that each spacecraft is at least 2 km from every other spacecraft in the chief NR plane as shown in Figure 3. Note that every initial mean main spacecraft MEE and nanosatellite ROE is the same for the 50 km and 35 km orbit scenarios except for the

main spacecraft semi-parameter. Under two-body acceleration only, all ROE remain constant, and the relative motion shown in Figure 3 is preserved for all time. However, the ROE vary under the influence of perturbations, and periodic station-keeping maneuvers are required to preserve the desired relative motion.[26,27,49,50] Station-keeping maneuvers are not considered in these case studies, and the relative motion is allowed to evolve naturally until the end of each simulation.

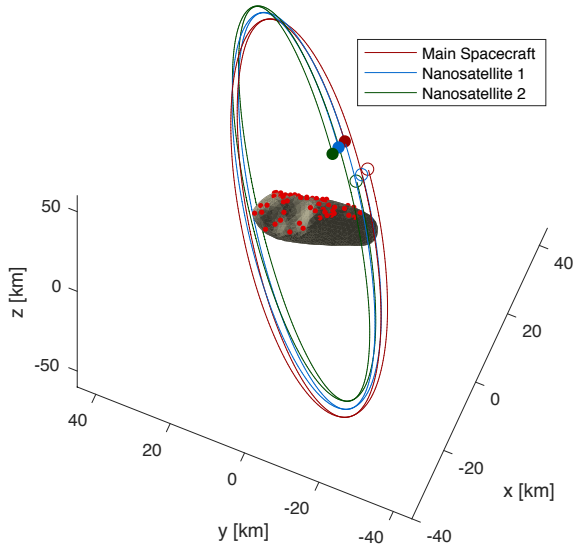

Figure 4: Motion of spacecraft swarm in ACI frame for the 50 km orbit scenario. The filled circles are spacecraft positions at the beginning of the simulation. Open circles are spacecraft positions just before the second orbit period is complete, and visible OpNav landmarks at that time are indicated by red points.

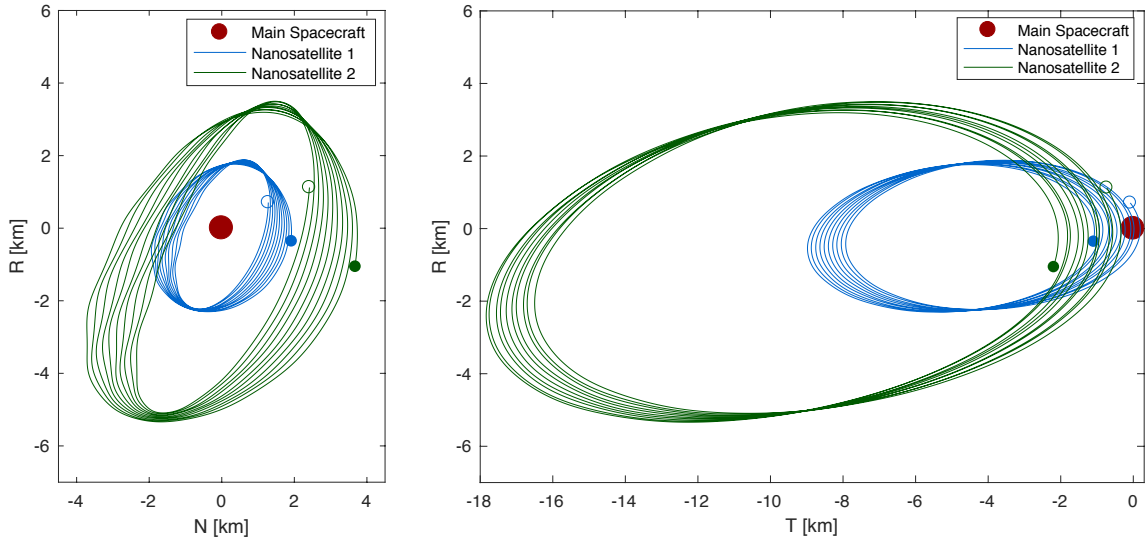

(a) NR plane

(b) TR plane

Figure 5: Motion of nanosatellites with respect to main spacecraft expressed in the main spacecraft RTN frame for the 50 km orbit scenario. The filled and open circles indicate positions at the beginning and end of the simulation respectively.

Figures 4 and 5 show the spacecraft motion for the 50 km orbit scenario. Figure 4 shows the motion of the spacecraft swarm relative to the asteroid expressed in the ACI frame as well as visible OpNav landmarks. OpNav landmarks are considered visible to all spacecraft if they are illuminated by direct sunlight, are not

blocked from the main spacecraft camera view by the asteroid, and are in the main spacecraft field of view (FOV). Note that there are no visible OpNav landmarks in shadowed regions of the asteroid in Figure 4. Figure 5 shows the motion of each nanosatellite with respect to the main spacecraft expressed in the chief RTN frame. The differences between the nominal motion shown in Figure 3 and the actual motion shown in Figure 5 are due mainly to the effects of J_2 and the fact that spacecraft separations are not small compared to the orbit radius.

Reference Truth

The dynamics of the asteroid and satellites are each treated as two body motion about the sun with perturbations on the asteroid orbit due to SRP and perturbations on the spacecraft orbit due to asteroid gravity and SRP. The asteroid and spacecraft orbits are simultaneously propagated through a high-accuracy variable step numerical integration of the fundamental orbit differential equation defined as

$$\ddot{\boldsymbol{r}}_{SA} = -\frac{\mu_\odot}{r_{SA}^3}\boldsymbol{r}_{SA} + \boldsymbol{f}_{A,SRP} \tag{36}$$

$$\ddot{\boldsymbol{r}}_{Sj} = -\frac{\mu_\odot}{r_{Sj}^3}\boldsymbol{r}_{Sj} - \frac{\mu}{r_j^3}\boldsymbol{r}_j + \boldsymbol{f}_G + \boldsymbol{f}_{j,SRP} \tag{37}$$

Here, $\mu_\odot$ is the sun gravitational parameter, $\boldsymbol{r}_{SA}$ is the vector from the sun to the asteroid, $\boldsymbol{r}_{Sj}$ is the vector from the sun to the jth spacecraft, and $\boldsymbol{r}_j$ is the vector pointing from the asteroid to the jth spacecraft. The vectors $\mathbf{f}_{A,SRP}$ and $\mathbf{f}_{j,SRP}$ are the SRP induced accelerations experienced by the asteroid and the jth spacecraft respectively. Accelerations due to SRP are computed using Eq. (6) where the radiation pressure coefficient and area-to-mass ratio of each spacecraft are 1.2 and 0.02 m^2/kg respectively.[39,51] In computing $\boldsymbol{f}_G$, the gravity coefficients recovered by the NEAR mission are used up to degree and order 10.[47] The orbital elements of Eros at the beginning of each simulation as well as other key Eros parameters are provided in Table 8.

Table 8: Case study orbital elements for Eros defined with respect to a sun centered inertial frame aligned with J2000 as well as other key Eros parameters.[47,52]

Orbital Elements				Key Parameters			
a	1.4583 AU	Ω	342.35°	α	11.363°	w	3.31x10^{-4} $\frac{\text{rad}}{\text{s}}$
e	0.22275	w	138.92°	δ	17.232°	μ	4.463x10^{-4} $\frac{\text{km}^3}{\text{s}^2}$
i	30.792°	M	119.97°	W_0	326.08°	R_{ref}	16 km

RF pseudo-range measurements are calculated using Eq. (11) where the geometric range is found by initializing τ as zero and completing three iterations of Eqs. (12) and (13). Doppler measurements are computed using Eq. (15) and the value of τ found while computing pseudo-range measurements. Optical measurements are calculated using Eq. (16), which simulates the true pixel measurements after they have been undistorted using the known camera distortion coefficients. Zero mean Gaussian noise is added to all measurements according to the uncertainties listed in Table 9. Noise is simulated in the star tracker measurements by multiplying the truth ACI to CF rotation matrices by 3-1-2 Euler angle rotation sequences. The rotation angles are zero mean random Gaussian variables with the standard deviations specified in Table 9, which are consistent with the Blue Canyon Technologies Nano-Star Camera.[53] The noisy star tracker measurements also create noise on the level of 0.1 mm in the pseudo-range measurements because the main spacecraft and nanosatellite RF antennas are placed at 1 m and 0.5 m from the spacecraft COM respectively. The main spacecraft camera has the same properties as the OSIRIS-REx NavCam,[54] and the nanosatellite camera parameters are consistent with the XCAM C3D CubeSat Camera[55] as seen in Table 10. Each spacecraft camera boresight points to the asteroid COM, and the camera frame y-axis is aligned with the spacecraft angular momentum vector.

Table 9: Measurement uncertainties (1-σ).

Inter-Satellite[16]		Landmark Tracking		Star Tracker[53]	
Range	10 cm	Main Spacecraft	0.5 px	Off-Axis	7 as
Doppler	1 mm/s	Nanosatellites	0.5 px	Roll	24 as

Table 10: Properties of the main spacecraft and nanosatellite cameras.

Camera	FOV [deg]	Number of Pixels	Focal Length [mm]	Pixel Size [μm]
Main Spacecraft[54]	44x33	2592x1944	7.6	2.2x2.2
Nanosatellites[55]	39x32	1280x1024	9.6	5.3x5.3

Results

First, filter convergence and accuracy results are presented followed by results on the reduction in computation time achieved through ETS. Filter convergence behavior for each mission architecture is compared for several parameters in Figure 6 for the 50 km orbit scenario. Each plot shows the filter estimated formal 3-σ uncertainty bound and the true error, which is the difference between the estimated and true state parameter values. Additional filter convergence plots are included in Appendix B. Note that the stereo architecture provides much faster convergence than the monocular architecture, especially for the nanosatellite MEE.

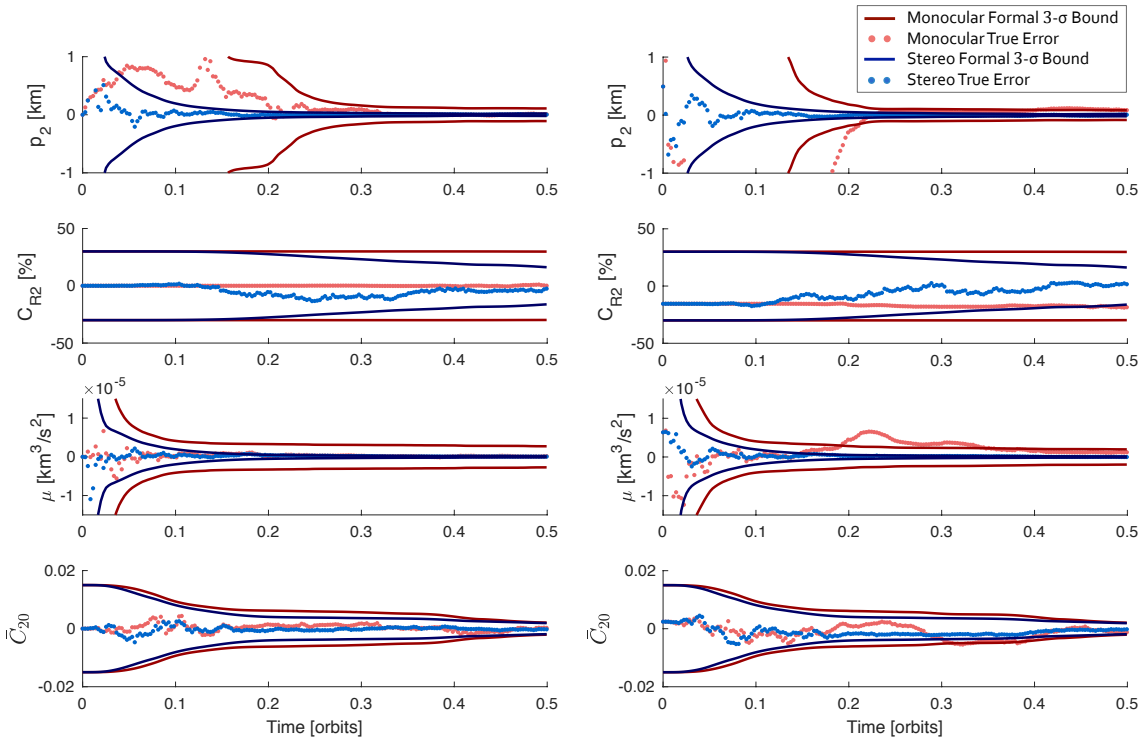

(a) Filter initialized with true state

(b) Filter initialized with state estimate error

Figure 6: Initial filter convergence behavior for the 50 km orbit scenario. The parameters p_2 and C_{R2} are the semi-parameter and radiation pressure coefficient respectively of the second spacecraft, which is the first nanosatellite.

The stereo mission architecture also achieves greater estimation accuracy and is more robust to the set of initial state estimate errors used in these simulations. Figure 14 shows the root mean square (RMS) true error of all the gravity coefficients for each degree averaged over the last half of an orbit for each simulation. When the filter is initialized with the true state, the stereo architecture is more accurate for gravity coefficients up

through degree six for the 50 km orbit scenario and is significantly more accurate for every degree for the 35 km orbit scenario. The mean absolute true error of the state parameters computed for the last half of an orbit of each simulation is shown in Table 11. Lines in Table 11 that include multiple state parameters are the average of the mean absolute true error of those parameters. Without initial state estimate errors, the stereo architecture error in spacecraft position and velocity as well as μ are as much as an order of magnitude smaller than that of the monocular architecture. As can be seen in Figure 14 and Table 11, the stereo architecture accuracy is similar whether the filter in the 50 km orbit scenario is initialized with the true state or with state estimate errors. In contrast, these same initial state estimate errors significantly degrade the accuracy of the monocular architecture.

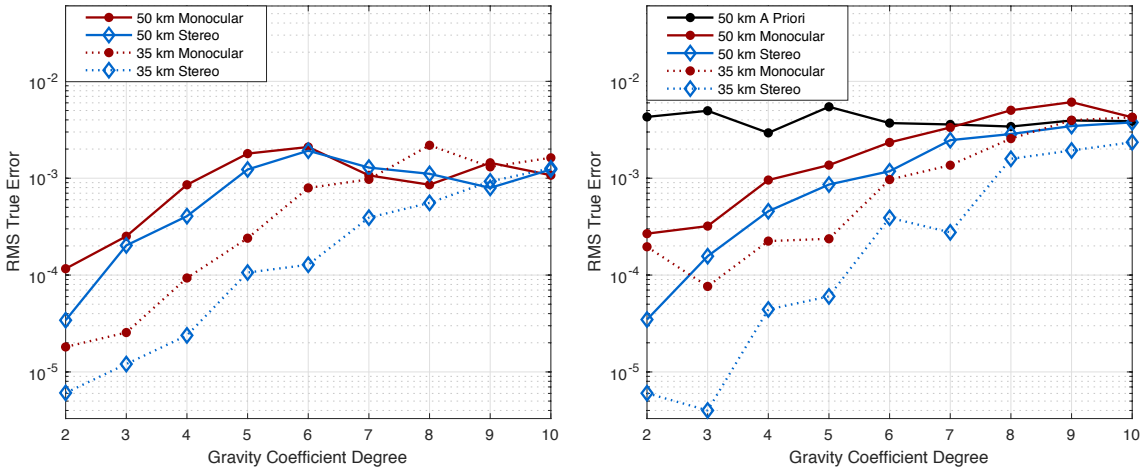

(a) Filter initialized with true state in 50 km orbit scenario

(b) Filter initialized with state error in 50 km orbit scenario

Figure 7: RMS true error of the estimated gravity coefficients averaged over the last half of an orbit for each mission architecture and orbit scenario. For the case of filter state estimate initialization error in the 50 km orbit scenario, the black line in (b) is the RMS true error of the initial state estimate provided to the filter.

Table 11: Mean absolute true error of the estimated state parameters computed over the last half of an orbit. In the 50 km orbit scenario, the filter was initialized with and without state error. Results are given by the numbers with and without parentheses respectively.

	50 km Orbit Scenario		35 km Orbit Scenario	
Parameter	Monocular	Stereo	Monocular	Stereo
μ [%]	1.18x10^{-2} (6.12x10^{-1})	1.72x10^{-3} (4.41x10^{-3})	2.52x10^{-3} (5.86x10^{-1})	1.17x10^{-4} (3.22x10^{-3})
S/C Position [m] $[x, y, z]$	1.07 (5.29x10^{1})	1.71x10^{-1} (5.07x10^{-1})	1.53x10^{-1} (3.72x10^{1})	8.37x10^{-2} (2.07x10^{-1})
S/C Velocity [mm/s] $[\dot{x}, \dot{y}, \dot{z}]$	6.36x10^{-2} (3.16)	1.71x10^{-2} (2.53x10^{-2})	3.12x10^{-2} (3.70)	1.08x10^{-2} (2.63x10^{-2})
*Landmark [m] $[L_x, L_y, L_z]$	4.86x10^{-1} (9.42)	3.16x10^{-1} (2.43x10^{-1})	3.80x10^{-1} (9.07)	2.42x10^{-1} (2.49x10^{-1})
r_{pm} [m]	3.78x10^{-1} (1.73x10^{1})	3.35x10^{-1} (5.29x10^{-2})	5.45x10^{-1} (1.72x10^{1})	1.49x10^{-1} (7.32x10^{-3})
ϕ_{pm} [deg]	2.77x10^{-2} (5.47x10^{-1})	2.63x10^{-3} (8.82x10^{-4})	4.21x10^{-2} (4.96x10^{-1})	1.78x10^{-3} (1.85x10^{-3})
α [deg]	1.12x10^{-4} (7.89x10^{-5})	1.69x10^{-4} (5.41x10^{-5})	1.02x10^{-4} (5.38x10^{-4})	8.26x10^{-5} (5.61x10^{-5})
δ [deg]	4.38x10^{-4} (1.62x10^{-4})	4.00x10^{-4} (1.98x10^{-5})	3.22x10^{-4} (5.68x10^{-4})	4.17x10^{-5} (1.29x10^{-4})
W_0 [deg]	4.28x10^{-3} (3.38x10^{-3})	2.72x10^{-3} (8.74x10^{-4})	5.02x10^{-3} (3.82x10^{-3})	2.96x10^{-3} (1.60x10^{-4})
w [%]	8.35x10^{-6} (4.69x10^{-6})	3.95x10^{-6} (5.17x10^{-6})	2.15x10^{-6} (2.90x10^{-6})	3.67x10^{-6} (4.05x10^{-6})
C_R [%]	1.90x10^{-1} (5.76x10^{-1})	4.81x10^{-2} (1.23x10^{-2})	2.12x10^{-2} (1.20x10^{-1})	1.92x10^{-2} (1.15x10^{-2})
b_{PR} [%]	1.72 (1.46x10^{1})	3.81 (1.0x10^{1})	7.51x10^{-1} (42.6)	1.38 (4.75)
b_D [%]	3.36x10^{-1} (4.76x10^{-1})	1.09 (6.32x10^{-1})	4.23x10^{-1} (1.68)	1.18 (7.25x10^{-1})

*Does not include six OpNav landmarks that were never visible because they are constantly shaded during the simulated time of year.

Additional simulations show that the spacecraft semi-parameters and μ are less observable for the monocular architecture than for the stereo architecture. The monocular architecture frequently converges on incorrect values of the spacecraft semi-parameters and μ while correctly estimating the other spacecraft MEEs. In this way, the MEE state effectively isolates the weakly observable part of the spacecraft state, which is the orbit size. Interestingly, the monocular architecture tends to either overestimate all the spacecraft semi-parameters and μ or to underestimate them all. Consider that the mean motion is proportional to μ and inversely proportional to the orbit semi-parameter. When the filter either overestimates or underestimates all the spacecraft semi-parameters and μ, the filter tends to still yield an accurate estimate of the mean motion, which is observable. In contrast, the orbit size and μ are very observable for the stereo architecture.

Using ETS, the filter takes about 2.8 seconds to complete both the time and measurement update at each filter call when run on a 2.8 GHz Intel Core i5-8400 processor using a MATLAB implementation. This is a 77% reduction in run time from the traditional UKF. Figure 8 (a) illustrates the utility of ETS by plotting the ratio of ETS-UKF to traditional UKF run time for the stereo architecture in these case studies as a function of the number of estimated OpNav landmark positions. The ETS-UKF run time is an even smaller fraction of the traditional UKF run time as the degree of the estimated gravity field decreases. Figure 8 (b) shows the ratio of ETS-UKF to UKF run time for these case studies if a degree and order five gravity field had been estimated. As can be seen in Figure 8 (b), ETS can decrease the run time by as much as an order of magnitude for some states.

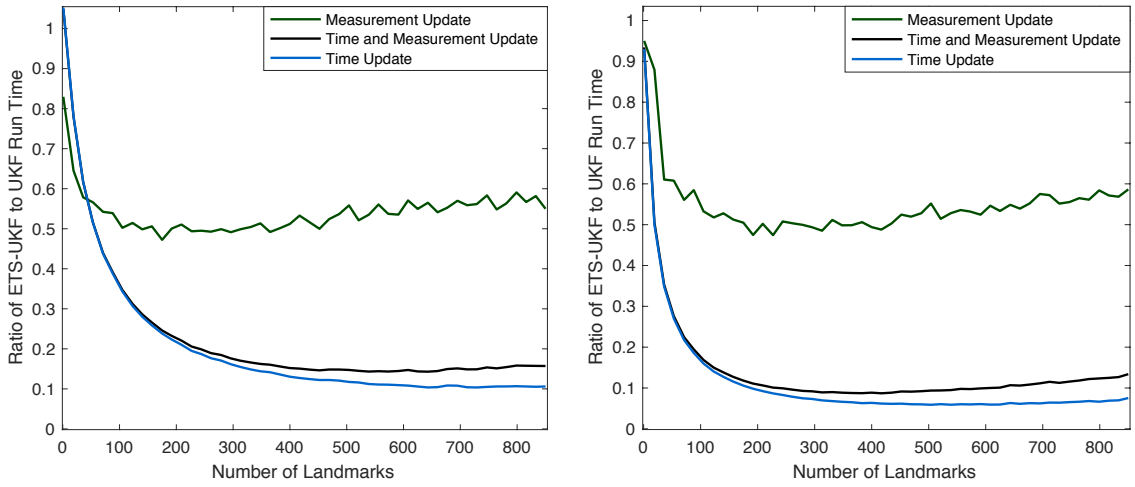

(a) Degree and order ten gravity field

(b) Degree and order five gravity field

Figure 8: Ratio of ETS-UKF to traditional UKF run time for the the stereo architecture in these case studies as a function of the number of estimated OpNav landmark positions assuming 20% of the OpNav landmarks are visible.

CONCLUSIONS

Asteroids are of interest for a variety of reasons including science, mining, and planetary defense. Completed asteroid missions have utilized a single, monolithic spacecraft and have depended extensively on ground-based systems. In contrast, this paper presents a novel mission and estimation architecture to simultaneously navigate and characterize an asteroid using a swarm of spacecraft with limited use of ground-based assets. The controllable swarm uses inter-spacecraft radio-frequency (RF) measurements and cooperative optical navigation. Measurements are processed in an unscented Kalman filter (UKF), which is more accurate and robust to initial state estimate errors for nonlinear systems than the extended Kalman filter (EKF) and does not require the computation of Jacobian matrices. Modified equinoctial elements (MEE) are employed for efficient numerical integration in the filter time update. Additionally, UKF run time is significantly reduced through a new technique of exploiting triangular structure (ETS) in the matrix square root in the UKF.

Case study results show that using multiple spacecraft instead of a single spacecraft to optically track asteroid landmarks provides more accurate estimation of the asteroid shape and gravity field, faster convergence, and more robustness to initial state estimate errors. Results also suggest that the proposed architecture achieves greater gravity recovery accuracy than autonomous asteroid characterization concepts in literature.[15–17] In the presented case studies, the proposed architecture gravity recovery accuracy was about five times worse than that of the NEAR mission. However, the NEAR solution was obtained by a batch estimator that simultaneously considered all the measurements for the entire year long mission while the presented case studies lasted for only ten or 20 orbits.[46,47] For the considered case studies, ETS reduced UKF run time by 77%. Furthermore, the ETS-UKF can be applied to any system with partially decoupled state parameter dynamics or any measurement that isn't a function of every state parameter. Results suggest the estimation algorithm may be implemented onboard, greatly reducing the need for ground-based estimation solutions and enabling the spacecraft to safely enter lower altitude orbits where the effects of gravity are more observable. Potentially, this could provide more accurate gravity recovery than ground-based missions. To further enable onboard implementation, swarm distributed processing will be investigated to alleviate the computational load on a single spacecraft.

Although the results of these first simulations are promising, sensitivity and Monte Carlo analyses will be performed to better characterize the performance of the proposed mission and estimation architecture over a wide variety of scenarios. Additionally, algorithms for feature correspondence will be researched. The reference truth will be modeled with higher fidelity, and either empirical accelerations or adaptive process noise will be utilized to handle accelerations that are included in the reference truth and not in the filter dynamics models. Future work will also include hardware-in-the-loop testing and validation using Stanford University's Space Rendezvous Laboratory (SLAB) high fidelity testbed. The ETS-UKF algorithm will be embedded on nanosatellite avionics to better test the feasibility of onboard implementation. Optical measurements will be simulated with a spacecraft camera observing both the SLAB optical stimulator and high resolution, additively manufactured model of 433 Eros.

APPENDIX A: EXPLOITING TRIANGULAR STRUCTURE EXAMPLES

Time Update Example

In this example, the filter state

$$\boldsymbol{x} = [\boldsymbol{MEE}^T \ \boldsymbol{L}^T]^T \tag{38}$$

is composed of the osculating MEE of a single spacecraft and the Cartesian ACAF position of a single OpNav landmark. The mean state estimate is given by

$$\boldsymbol{\mu} = [\bar{p} \ \ \bar{f} \ \ \bar{g} \ \ \bar{h} \ \ \bar{k} \ \ \bar{l} \ \ \bar{L}_x \ \ \bar{L}_y \ \ \bar{L}_z]^T \tag{39}$$

and the 19 sigma points are

$$
\begin{array}{ccccccc}
\boldsymbol{\chi}_{[0]} & \boldsymbol{\chi}_{[1]} & \boldsymbol{\chi}_{[2]} & \boldsymbol{\chi}_{[3]} & \boldsymbol{\chi}_{[7]} & \boldsymbol{\chi}_{[8]} & \boldsymbol{\chi}_{[9]} \\
\begin{bmatrix} \bar{p} \\ \bar{f} \\ \bar{g} \\ \bar{h} \\ \bar{k} \\ \bar{l} \\ \bar{L}_x \\ \bar{L}_y \\ \bar{L}_z \end{bmatrix} ,
\begin{bmatrix} \bar{p}+A_{1,1} \\ \bar{f}+A_{2,1} \\ \bar{g}+A_{3,1} \\ \bar{h}+A_{4,1} \\ \bar{k}+A_{5,1} \\ \bar{l}+A_{6,1} \\ \bar{L}_x+A_{7,1} \\ \bar{L}_y+A_{8,1} \\ \bar{L}_z+A_{9,1} \end{bmatrix} ,
\begin{bmatrix} \bar{p} \\ \bar{f}+A_{2,2} \\ \bar{g}+A_{3,2} \\ \bar{h}+A_{4,2} \\ \bar{k}+A_{5,2} \\ \bar{l}+A_{6,2} \\ \bar{L}_x+A_{7,2} \\ \bar{L}_y+A_{8,2} \\ \bar{L}_z+A_{9,2} \end{bmatrix} ,
\begin{bmatrix} \bar{p} \\ \bar{f} \\ \bar{g}+A_{3,3} \\ \bar{h}+A_{4,3} \\ \bar{k}+A_{5,3} \\ \bar{l}+A_{6,3} \\ \bar{L}_x+A_{7,3} \\ \bar{L}_y+A_{8,3} \\ \bar{L}_z+A_{9,3} \end{bmatrix} ,\ldots,
\begin{bmatrix} \bar{p} \\ \bar{f} \\ \bar{g} \\ \bar{h} \\ \bar{k} \\ \bar{l} \\ \bar{L}_x+A_{7,7} \\ \bar{L}_y+A_{8,7} \\ \bar{L}_z+A_{9,7} \end{bmatrix}
\begin{bmatrix} \bar{p} \\ \bar{f} \\ \bar{g} \\ \bar{h} \\ \bar{k} \\ \bar{l} \\ \bar{L}_x \\ \bar{L}_y+A_{8,8} \\ \bar{L}_z+A_{9,8} \end{bmatrix}
\begin{bmatrix} \bar{p} \\ \bar{f} \\ \bar{g} \\ \bar{h} \\ \bar{k} \\ \bar{l} \\ \bar{L}_x \\ \bar{L}_y \\ \bar{L}_z+A_{9,9} \end{bmatrix}
\end{array}
$$

$$
\begin{array}{ccccccc}
\boldsymbol{\chi}_{[10]} & \boldsymbol{\chi}_{[11]} & \boldsymbol{\chi}_{[12]} & \boldsymbol{\chi}_{[16]} & \boldsymbol{\chi}_{[17]} & \boldsymbol{\chi}_{[18]} \\
\begin{bmatrix} \bar{p}-A_{1,1} \\ \bar{f}-A_{2,1} \\ \bar{g}-A_{3,1} \\ \bar{h}-A_{4,1} \\ \bar{k}-A_{5,1} \\ \bar{l}-A_{6,1} \\ \bar{L}_x-A_{7,1} \\ \bar{L}_y-A_{8,1} \\ \bar{L}_z-A_{9,1} \end{bmatrix} ,
\begin{bmatrix} \bar{p} \\ \bar{f}-A_{2,2} \\ \bar{g}-A_{3,2} \\ \bar{h}-A_{4,2} \\ \bar{k}-A_{5,2} \\ \bar{l}-A_{6,2} \\ \bar{L}_x-A_{7,2} \\ \bar{L}_y-A_{8,2} \\ \bar{L}_z-A_{9,2} \end{bmatrix} ,
\begin{bmatrix} \bar{p} \\ \bar{f} \\ \bar{g}-A_{3,3} \\ \bar{h}-A_{4,3} \\ \bar{k}-A_{5,3} \\ \bar{l}-A_{6,3} \\ \bar{L}_x-A_{7,3} \\ \bar{L}_y-A_{8,3} \\ \bar{L}_z-A_{9,3} \end{bmatrix} ,\ldots,
\begin{bmatrix} \bar{p} \\ \bar{f} \\ \bar{g} \\ \bar{h} \\ \bar{k} \\ \bar{l} \\ \bar{L}_x-A_{7,7} \\ \bar{L}_y-A_{8,7} \\ \bar{L}_z-A_{9,7} \end{bmatrix}
\begin{bmatrix} \bar{p} \\ \bar{f} \\ \bar{g} \\ \bar{h} \\ \bar{k} \\ \bar{l} \\ \bar{L}_x \\ \bar{L}_y-A_{8,8} \\ \bar{L}_z-A_{9,8} \end{bmatrix}
\begin{bmatrix} \bar{p} \\ \bar{f} \\ \bar{g} \\ \bar{h} \\ \bar{k} \\ \bar{l} \\ \bar{L}_x \\ \bar{L}_y \\ \bar{L}_z-A_{9,9} \end{bmatrix}
\end{array}
$$

where $A_{i,j}$ is the element from the ith row and j^{th} column of $\mathbf{A}$.

The traditional UKF would require each sigma point to be passed through the nonlinear filter dynamics model, which would result in nineteen orbit propagations. However, note that the spacecraft dynamics are independent from the OpNav landmark position and that sigma points 7-9 and 16-18 are only different from the zeroth sigma point in the OpNav landmark position. The orbit propagation for sigma points 0, 7-9, and 16-18 will be exactly the same. Instead of recomputing the orbit propagation for each of these points, the orbit propagation from the zeroth sigma point can be reused for sigma points 7-9 and 16-18.

Instead of nineteen orbit propagations, the ETS-UKF only requires 13. As more landmarks are added to the state vector, the ETS-UKF continues to require 13 orbit propagations while the traditional UKF requires six more orbit propagations for each additional landmark.

Measurement Update Example

In this example, the filter state

$$
\boldsymbol{x} = [\boldsymbol{MEE}^T \ {}^{\boldsymbol{v}}\boldsymbol{L}^T \ {}^{\boldsymbol{h}}\boldsymbol{L}^T \ \mu]^T \tag{40}
$$

is composed of the MEE of a single spacecraft, the Cartesian ACAF positions of two OpNav landmarks, and the asteroid gravitational parameter. One OpNav landmark is visible and the other is hidden as indicated by the superscripts v and h respectively. The mean state is

$$
\boldsymbol{\mu} = [\bar{p} \ \bar{f} \ \bar{g} \ \bar{h} \ \bar{k} \ \bar{l} \ {}^{v}\bar{L}_x \ {}^{v}\bar{L}_y \ {}^{v}\bar{L}_z \ {}^{h}\bar{L}_x \ {}^{h}\bar{L}_y \ {}^{h}\bar{L}_z \ \bar{\mu}]^T \tag{41}
$$

and the 27 sigma points are

$$
\begin{array}{cccccc}
\boldsymbol{\chi}_{[0]} & \boldsymbol{\chi}_{[1]} & \boldsymbol{\chi}_{[2]} & \boldsymbol{\chi}_{[11]} & \boldsymbol{\chi}_{[12]} & \boldsymbol{\chi}_{[13]} \\
\begin{bmatrix} \bar{p} \\ \bar{f} \\ \bar{g} \\ \bar{h} \\ \bar{k} \\ \bar{l} \\ {}^{v}\bar{L}_x \\ {}^{v}\bar{L}_y \\ {}^{v}\bar{L}_z \\ {}^{h}\bar{L}_x \\ {}^{h}\bar{L}_y \\ {}^{h}\bar{L}_z \\ \bar{\mu} \end{bmatrix}, &
\begin{bmatrix} \bar{p} + A_{1,1} \\ \bar{f} + A_{2,1} \\ \bar{g} + A_{3,1} \\ \bar{h} + A_{4,1} \\ \bar{k} + A_{5,1} \\ \bar{l} + A_{6,1} \\ {}^{v}\bar{L}_x + A_{7,1} \\ {}^{v}\bar{L}_y + A_{8,1} \\ {}^{v}\bar{L}_z + A_{9,1} \\ {}^{h}\bar{L}_x + A_{10,1} \\ {}^{h}\bar{L}_y + A_{11,1} \\ {}^{h}\bar{L}_z + A_{12,1} \\ \bar{\mu} + A_{13,1} \end{bmatrix}, &
\begin{bmatrix} \bar{p} \\ \bar{f} + A_{2,2} \\ \bar{g} + A_{3,2} \\ \bar{h} + A_{4,2} \\ \bar{k} + A_{5,2} \\ \bar{l} + A_{6,2} \\ {}^{v}\bar{L}_x + A_{7,2} \\ {}^{v}\bar{L}_y + A_{8,2} \\ {}^{v}\bar{L}_z + A_{9,2} \\ {}^{h}\bar{L}_x + A_{10,2} \\ {}^{h}\bar{L}_y + A_{11,2} \\ {}^{h}\bar{L}_z + A_{12,2} \\ \bar{\mu} + A_{13,2} \end{bmatrix}, \ldots, &
\begin{bmatrix} \bar{p} \\ \bar{f} \\ \bar{g} \\ \bar{h} \\ \bar{k} \\ \bar{l} \\ {}^{v}\bar{L}_x \\ {}^{v}\bar{L}_y \\ {}^{v}\bar{L}_z \\ {}^{h}\bar{L}_x \\ {}^{h}\bar{L}_y + A_{11,11} \\ {}^{h}\bar{L}_z + A_{12,11} \\ \bar{\mu} + A_{13,11} \end{bmatrix}, &
\begin{bmatrix} \bar{p} \\ \bar{f} \\ \bar{g} \\ \bar{h} \\ \bar{k} \\ \bar{l} \\ {}^{v}\bar{L}_x \\ {}^{v}\bar{L}_y \\ {}^{v}\bar{L}_z \\ {}^{h}\bar{L}_x \\ {}^{h}\bar{L}_y \\ {}^{h}\bar{L}_z + A_{12,12} \\ \bar{\mu} + A_{13,12} \end{bmatrix}, &
\begin{bmatrix} \bar{p} \\ \bar{f} \\ \bar{g} \\ \bar{h} \\ \bar{k} \\ \bar{l} \\ {}^{v}\bar{L}_x \\ {}^{v}\bar{L}_y \\ {}^{v}\bar{L}_z \\ {}^{h}\bar{L}_x \\ {}^{h}\bar{L}_y \\ {}^{h}\bar{L}_z \\ \bar{\mu} + A_{13,13} \end{bmatrix}
\end{array}
$$

$$
\begin{array}{cccccc}
\boldsymbol{\chi}_{[14]} & \boldsymbol{\chi}_{[15]} & \boldsymbol{\chi}_{[24]} & \boldsymbol{\chi}_{[25]} & \boldsymbol{\chi}_{[26]} \\
\begin{bmatrix} \bar{p} - A_{1,1} \\ \bar{f} - A_{2,1} \\ \bar{g} - A_{3,1} \\ \bar{h} - A_{4,1} \\ \bar{k} - A_{5,1} \\ \bar{l} - A_{6,1} \\ {}^{v}\bar{L}_x - A_{7,1} \\ {}^{v}\bar{L}_y - A_{8,1} \\ {}^{v}\bar{L}_z - A_{9,1} \\ {}^{h}\bar{L}_x - A_{10,1} \\ {}^{h}\bar{L}_y - A_{11,1} \\ {}^{h}\bar{L}_z - A_{12,1} \\ \bar{\mu} - A_{13,1} \end{bmatrix}, &
\begin{bmatrix} \bar{p} \\ \bar{f} - A_{2,2} \\ \bar{g} - A_{3,2} \\ \bar{h} - A_{4,2} \\ \bar{k} - A_{5,2} \\ \bar{l} - A_{6,2} \\ {}^{v}\bar{L}_x - A_{7,2} \\ {}^{v}\bar{L}_y - A_{8,2} \\ {}^{v}\bar{L}_z - A_{9,2} \\ {}^{h}\bar{L}_x - A_{10,2} \\ {}^{h}\bar{L}_y - A_{11,2} \\ {}^{h}\bar{L}_z - A_{12,2} \\ \bar{\mu} - A_{13,2} \end{bmatrix}, \ldots, &
\begin{bmatrix} \bar{p} \\ \bar{f} \\ \bar{g} \\ \bar{h} \\ \bar{k} \\ \bar{l} \\ {}^{v}\bar{L}_x \\ {}^{v}\bar{L}_y \\ {}^{v}\bar{L}_z \\ {}^{h}\bar{L}_x \\ {}^{h}\bar{L}_y - A_{11,11} \\ {}^{h}\bar{L}_z - A_{12,11} \\ \bar{\mu} - A_{13,11} \end{bmatrix}, &
\begin{bmatrix} \bar{p} \\ \bar{f} \\ \bar{g} \\ \bar{h} \\ \bar{k} \\ \bar{l} \\ {}^{v}\bar{L}_x \\ {}^{v}\bar{L}_y \\ {}^{v}\bar{L}_z \\ {}^{h}\bar{L}_x \\ {}^{h}\bar{L}_y \\ {}^{h}\bar{L}_z - A_{12,12} \\ \bar{\mu} - A_{13,12} \end{bmatrix}, &
\begin{bmatrix} \bar{p} \\ \bar{f} \\ \bar{g} \\ \bar{h} \\ \bar{k} \\ \bar{l} \\ {}^{v}\bar{L}_x \\ {}^{v}\bar{L}_y \\ {}^{v}\bar{L}_z \\ {}^{h}\bar{L}_x \\ {}^{h}\bar{L}_y \\ {}^{h}\bar{L}_z \\ \bar{\mu} - A_{13,13} \end{bmatrix}
\end{array}
$$

For the given state, a single set of optical measurements of the visible landmark are available at each filter call. The traditional UKF mechanization would require the computation of 27 sets of optical measurements, one for each sigma point. However, note that the pixel measurements for sigma points 0, 10-13, and 23-26 are the same. A change in the position of a hidden OpNav landmark or the value of the asteroid gravitational parameter does not affect optical measurements of the visible OpNav landmark.

The ETS-UKF only requires 19 pixel measurements because the pixel measurements from the zeroth sigma point can be reused for sigma points 10-13 and 23-26. The number of optical measurements required by the ETS-UKF is constant as more hidden OpNav landmarks and gravity parameters are added to the state.

APPENDIX B: ADDITIONAL FILTER CONVERGENCE RESULTS

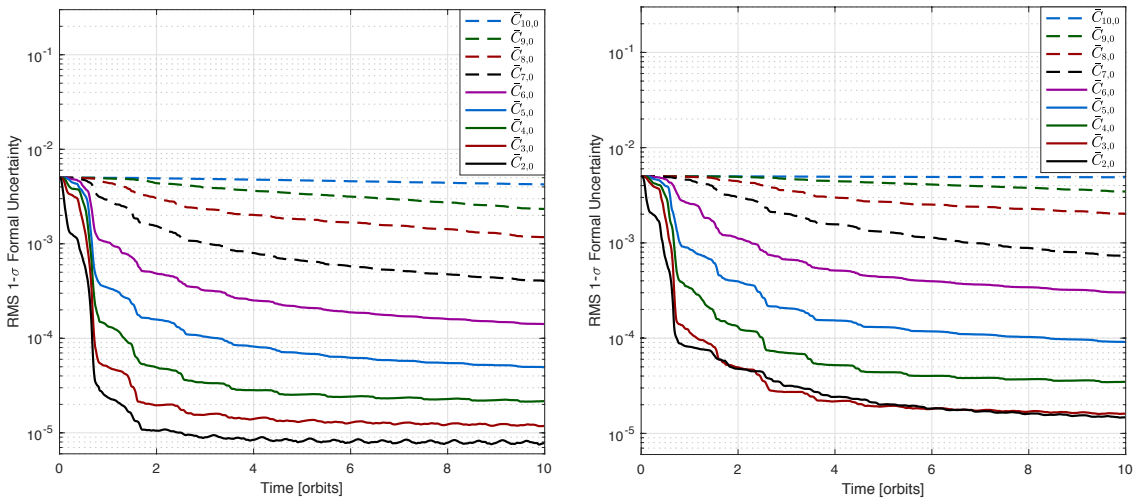

(a) Stereo mission architecture (b) Monocular mission architecture

Figure 9: RMS 1-σ formal uncertainty of the estimated zonal gravity coefficients for the 50 km orbit scenario where the filter was initialized with the true state. Note that the stereo architecture provides faster convergence.

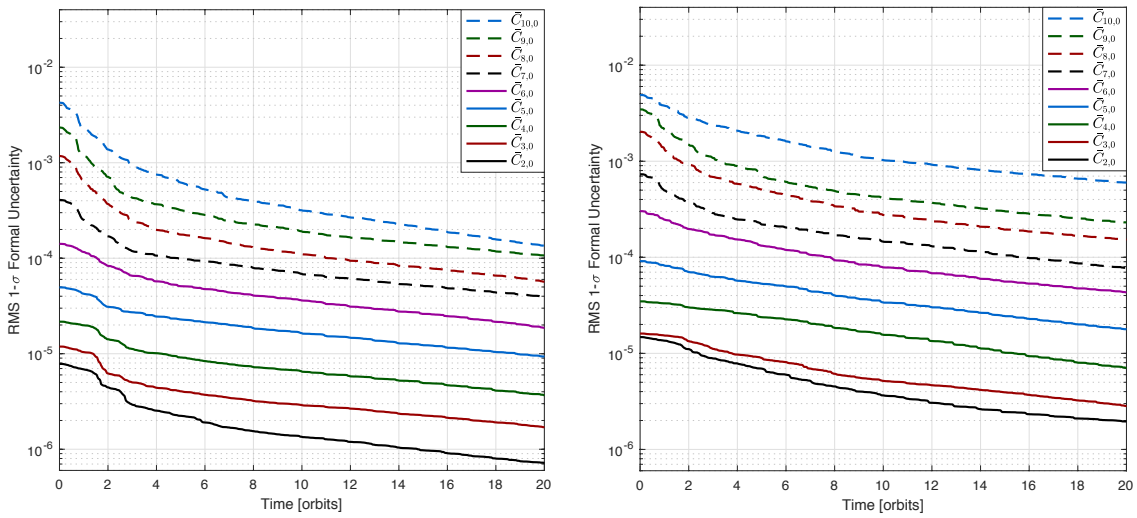

(a) Stereo mission architecture (b) Monocular mission architecture

Figure 10: RMS 1-σ formal uncertainty of the estimated zonal gravity coefficients for the 35 km orbit scenario where the filter was initialized with the true state in the 50 km orbit scenario. Note that the stereo architecture provides faster convergence.

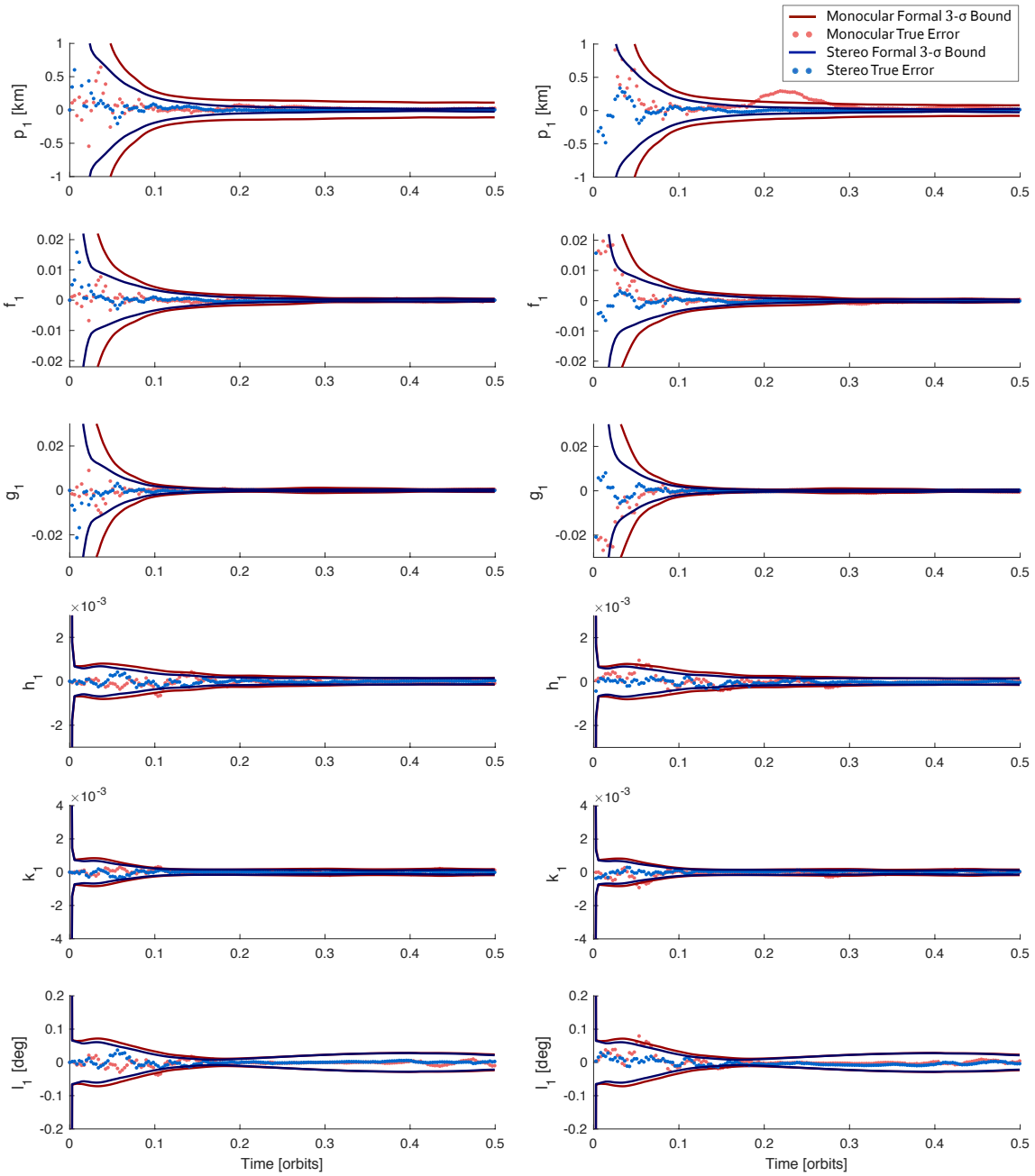

(a) Filter initialized with true state

(b) Filter initialized with mean state estimate error

Figure 11: Initial filter convergence of the main spacecraft MEE for the 50 km orbit scenario. The stereo architecture converges more quickly for the first three MEE. For the last three MEE, the performance is similar for the stereo and monocular architectures.

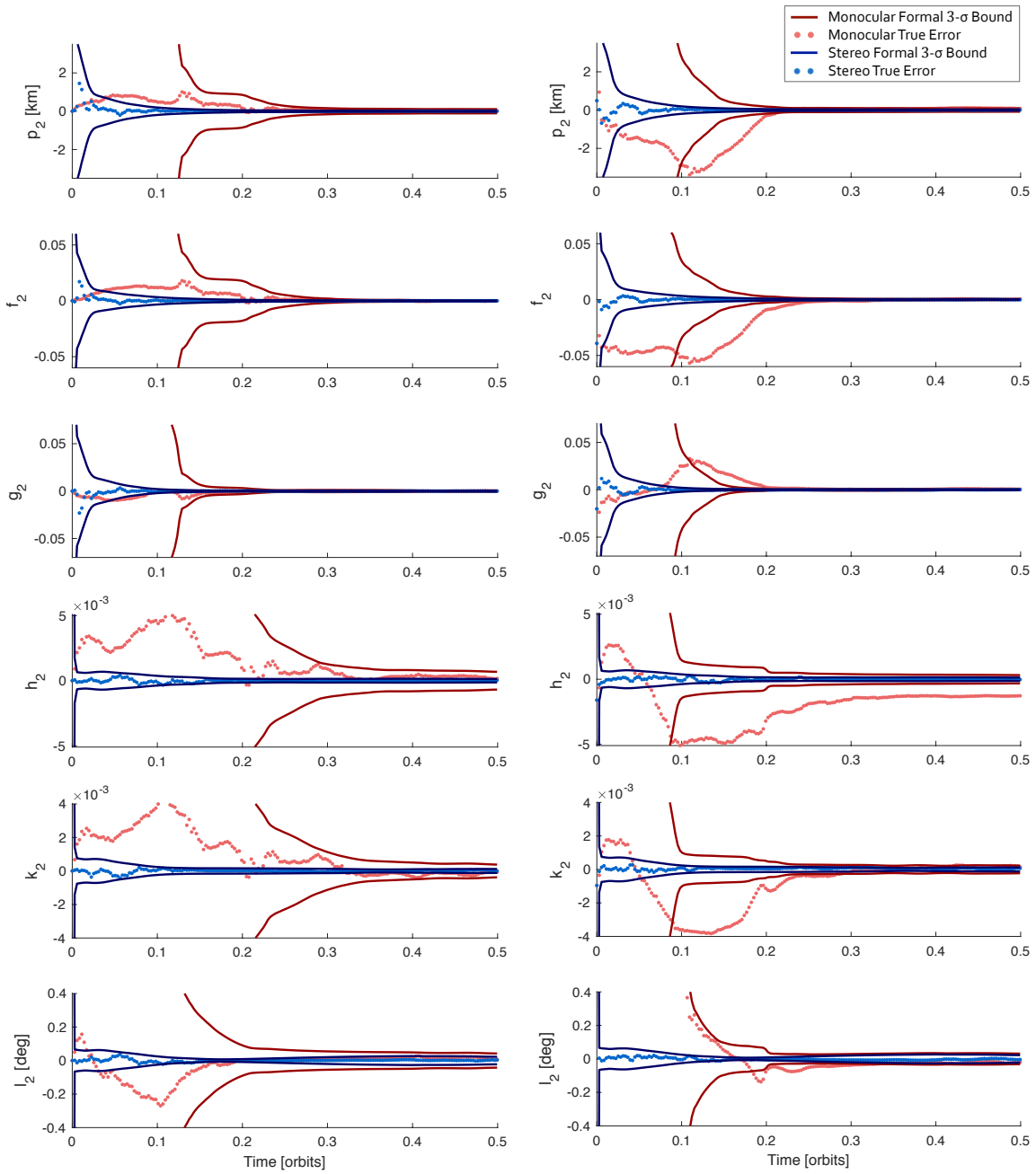

(a) Filter initialized with true state

(b) Filter initialized with mean state estimate error

Figure 12: Initial filter convergence for the first nanosatellite MEE for the 50 km orbit scenario. The stereo architecture provides much faster and more stable convergence.

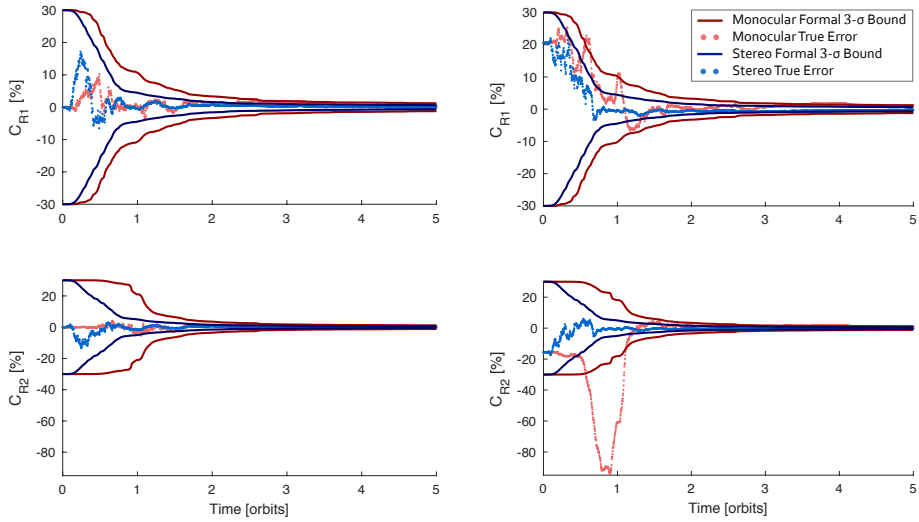

(a) Filter initialized with true state (b) Filter initialized with mean state estimate error

Figure 13: Initial filter convergence for the radiation pressure coefficients of the first and second spacecraft, which are the main spacecraft and first nanosatellite respectively. The stereo architecture converges much more quickly, especially for the first nanosatellite.

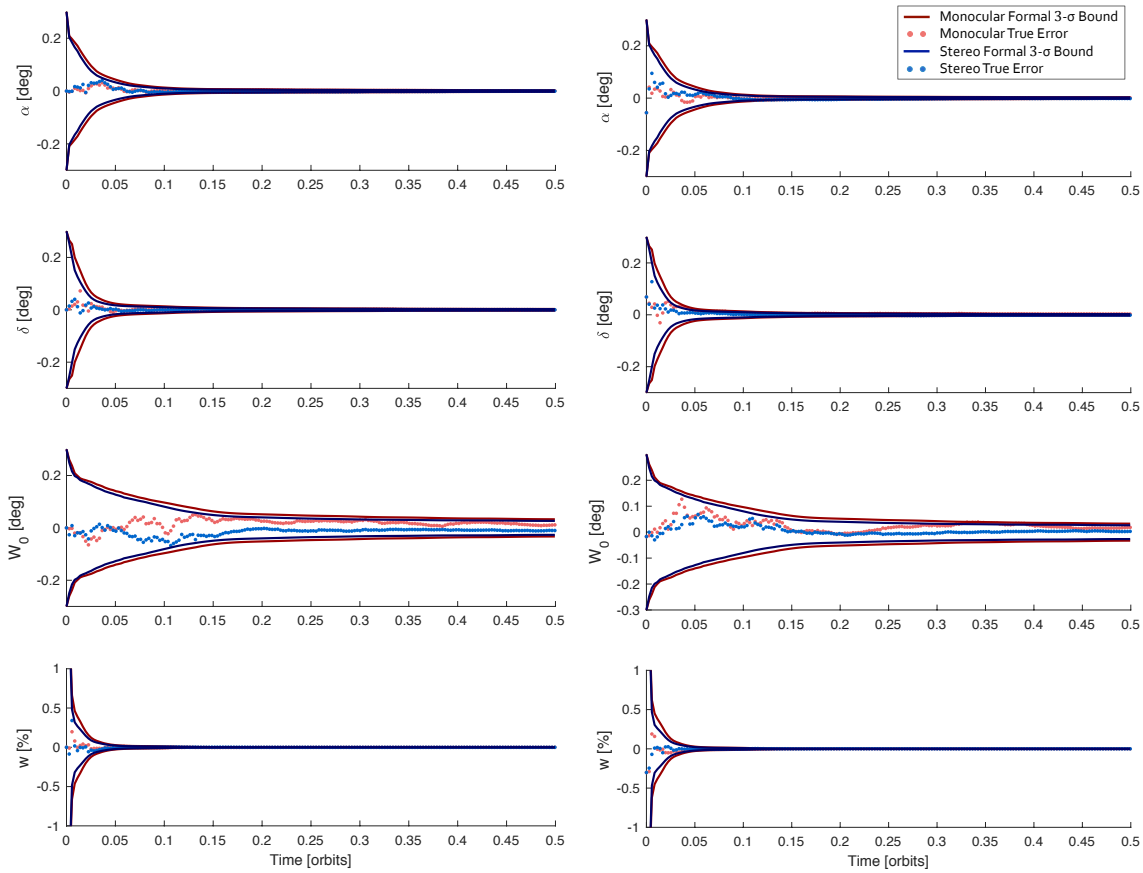

(a) Filter initialized with true state (b) Filter initialized with mean state estimate error

Figure 14: Initial filter convergence for the estimated asteroid attitude parameters for the 50 km orbit scenario. The stereo architecture converges only slightly faster.

ACKNOWLEDGEMENTS

This material is based upon work supported by the National Science Foundation Graduate Research Fellowship Program under Grant No. DGE-1656518. Any opinions, findings, and conclusions or recommendations expressed in this material are those of the authors and do not necessarily reflect the views of the National Science Foundation. This research is also part of the Autonomous Nanosatellite Swarming (ANS) Using Radio-Frequency and Optical Navigation project supported by the NASA Small Spacecraft Technology Program cooperative agreement number 80NSSC18M0058.

REFERENCES

[1] National Research Council, *Vision and Voyages for Planetary Science in the Decade 2013-2022*. 2011, doi:10.17226/13117.

[2] A. Coradini, D. Turrini, C. Federico, and G. Magni, "Vesta and Ceres: Crossing the History of the Solar System," *Space Science Reviews*, Vol. 163, No. 1, 2011, pp. 25–40, doi:10.1007/s11214-011-9792-x.

[3] Y. Takahashi, "Gravity Field Characterization Around Small Bodies," *University of Colorado Boulder, PhD Thesis*, 2013.

[4] D. D. Mazanek, R. G. Merrill, J. R. Brophy, and R. P. Mueller, "Asteroid Redirect Mission Concept: A Bold Approach for Utilizing Space Resources," *Acta Astronautica*, Vol. 117, 2015, pp. 163–171, doi:10.1016/j.actaastro.2015.06.018.

[5] W. Owen, T. C. Wang, A. Harch, M. Bell, and C. Peterson, "NEAR Optical Navigation at Eros," *AAS/AIAA Astrodynamics Specialist Conference*, 2001.

[6] N. Mastrodemos, B. Rush, A. Vaughan, and O. William, "Optical Navigation for the Dawn Mission at Vesta," *23rd International Symposium on Space Flight Dynamics, Pasadena, CA*, 2012.

[7] T. Hashimoto, T. Kubota, J. Kawaguchi, M. Uo, K. Shirakawa, T. Kominato, and H. Morita, "Vision-Based Guidance, Navigation, and Control of Hayabusa Spacecraft - Lessons Learned From Real Operation," *IFAC Proceedings Volumes*, Vol. 43, No. 15, 2010, doi:10.3182/20100906-5-JP-2022.00045.

[8] D. Lauretta et al, "OSIRIS-REx: Sample Return from Asteroid (101955) Bennu," *Space Science Reviews*, Vol. 212, No. 1, 2017, pp. 925–984, doi:10.1007/s11214-017-0405-1.

[9] Y. Tsuda, M. Yoshikawa, T. Saiki, S. Nakazawa, and S.-i. Watanabe, "Hayabusa2–Sample Return and Kinetic Impact Mission to Near-Earth Asteroid Ryugu," *Acta Astronautica*, Jan. 2018, 10.1016/j.actaastro.2018.01.030.

[10] B. G. Williams, "Technical Challenges and Results for Navigation of NEAR Shoemaker," *Johns Hopkins APL Technical Digest*, Vol. 23, No. 1, 2002.

[11] C.Polanskey, S. Joy, and C. Raymond, "Dawn Science Planning, Operations and Archiving," *Space Science Reviews*, Vol. 163, No. 1, 2011, pp. 511–543, doi:10.1007/s11214-011-9855-z.

[12] J. A. Atchison, R. H. Mitch, C. Apland, C. L. Kee, and K. W. Harclerode, "Small body in-situ Multi-probe Mass Estimation Experiment (SIMMEE)," *2017 IEEE Aerospace Conference*, 2017, 10.1109/AERO.2017.7943741.

[13] A. Cheng, A. Rivkin, P. Michel, C. Lisse, K. Walsh, D. Ragozzine, C. Chapman, W. Merline, and L. Benner, "Binary and Multiple Systems," *Johns Hopkins University Applied Physics Laboratory*, 2009.

[14] A. S. Konopliv, S. W. Asmar, B. G. Bills, N. Mastrodemos, R. S. Park, C. A. Raymond, D. E. Smith, and M. T. Zuber, "The Dawn Gravity Investigation at Vesta and Ceres," *Space Science Reviews*, Vol. 163, No. 1, 2011, pp. 461–486, doi:10.1007/s11214-011-9794-8.

[15] J. Leonard, B. Jones, E. Villalba, and G. Born, "Absolute Orbit Determination and Gravity Field Recovery for 433 Eros Using Satellite-to-Satellite Tracking," American Institute of Aeronautics and Astronautics, 2012, doi:10.2514/6.2012-4877.

[16] S. Hesar, J. Parker, J. McMahon, and G. Born, "Small Body Gravity Field Estimation Using LIAISON Suplemented Optical Navigation," *AAS GN&C Conference*, 2015.

[17] K. Fujimoto, N. Stacey, and J. M. Turner, "Stereoscopic Image Velocimetry as a Measurement Type for Autonomous Asteroid Gravimetry," American Institute of Aeronautics and Astronautics, 2016, doi:10.2514/6.2016-5566.

[18] M. L. Psiaki, "Absolute Orbit and Gravity Determination Using Relative Position Measurements Between Two Satellites," *Journal of Guidance, Control, and Dynamics*, Vol. 34, No. 5, 2011, pp. 1285–1297, 10.2514/1.47560.

[19] J. Atchison, R. Mitch, and A. Rivkin, "Swarm Flyby Gravimetry," *The Johns Hopkins University Applied Physics Laboratory, NIAC Phase I Final Report*, 2015.

[20] J. Atchison et al., "Swarm Flyby Gravimetry," *The Johns Hopkins University Applied Physics Laboratory, NIAC Phase II Final Report*, 2017.

[21] J. H. Taylor, "The Cramer-Rao Estimation Error Lower Bound Computation for Deterministic Nonlinear Systems," *1978 IEEE Conference on Decision and Control including the 17th Symposium on Adaptive Processes*, 1978, pp. 1178–1181, doi:10.1109/CDC.1978.268121.

[22] S. D'Amico, "Autonomous Nanosatellite Swarming (ANS) Using Radio-Frequency and Optical Navigation; NASA Fact Sheet, Stanford Space Rendezvous Laboratory (SLAB)," `https://damicos.people.stanford.edu/sites/g/files/sbiybj2226/f/ans_factsheet_6-21-18.pdf`, 2018.

[23] D. J. Scheeres, *Orbital Motion in Strongly Perturbed Environments: Applications to Asteroid, Comet and Planetary Satellite Orbiters*. Springer, 2016.

[24] J. A. Burns and V. S. Safronov, "Asteroid Nutation Angles," *Monthly Notices of the Royal Astronomical Society*, Vol. 165, 1973, p. 403, doi:10.1093/mnras/165.4.403.

[25] R. W. Gaskell, O. S. Barnouin-Jha, D. J. Scheeres, A. S. Konopliv, T. Mukai, S. Abe, J. Saito, M. Ishiguro, T. Kubota, T. Hashimoto, J. Kawaguchi, M. Yoshikawa, K. Shirakawa, T. Kominato, N. Hirata, and H. Demura, "Characterizing and Navigating Small Bodies with Imaging Data," *Meteoritics & Planetary Science Archives*, Vol. 43, No. 6, 2008, pp. 1049–1061.

[26] S. D'Amico, "Autonomous Formation Flying in Low Earth Orbit.," *PhD Thesis, Ridderprint*, 2010. OCLC: 839641932.

[27] A. W. Koenig and S. D'Amico, "Robust and Safe N-Spacecraft Swarming in Perturbed Near-Circular Orbits," *Journal of Guidance, Control, and Dynamics*, Vol. 41, No. 8, 2018, pp. 1643–1662, doi:10.2514/1.G003249.

[28] S. J. Julier and J. K. Uhlmann, "New Extension of the Kalman Filter to Nonlinear Systems," *Signal Processing, Sensor Fusion, and Target Recognition VI*, Vol. 3068, 1997, pp. 182–194, doi:10.1117/12.280797.

[29] C. Frost, "Small Spacecraft Technology State of the Art," *NASA Ames Research Center*, 2015.

[30] T. M. Lovelly and A. D. George, "Comparative Analysis of Present and Future Space-Grade Processors with Device Metrics," *Journal of Aerospace Information Systems*, Vol. 14, No. 3, 2017-03-01, pp. 184–197, doi:10.2514/1.I010472.

[31] B. Archinal, "Report of the IAU Working Group on Cartographic Coordinates and Rotational Elements: 2009," *Celestial Mechanics and Dynamical Astronomy*, Vol. 109, No. 2, 2011, pp. 101–135, doi:10.1007/s10569-010-9320-4.

[32] M. Walker, B. Ireland, and J. Owens, "A Set of Modified Equinoctial Orbit Elements," *Celestial Mechanics*, Vol. 36, No. 4, 1985, pp. 409–419, doi:10.1007/BF01227493.

[33] J. Sullivan, T. Lovell, and S. D'Amico, "Angles-Only Navigation for Autonomous On-Orbit Space Situational Awareness Applications," *AAS/AIAA Astrodynamics Specialist Conference, Snowbird, UT*, 2018.

[34] J. Sullivan and S. D'Amico, "Nonlinear Kalman Filtering for Improved Angles-Only Navigation Using Relative Orbital Elements," *Journal of Guidance, Control, and Dynamics*, Vol. 40, No. 9, 2017, pp. 2183–2200, doi:10.2514/1.G002719.

[35] J. L. Read, "Modified Chebyshev Picard Iteration: Integration of Perturbed Motion Using Modified Equinoctial Elements," *Texas A&M University, PhD Thesis*, 2016.

[36] D. A. Vallado and W. D. McClain, *Fundamentals of Astrodynamics and Applications*. Microcosm Press/Springer, 4th ed., 2007.

[37] R. A. Werner and D. J. Scheeres, "Exterior Gravitation of a Polyhedron Derived and Compared with Harmonic and Mascon Gravitation Representations of Asteroid 4769 Castalia," *Celestial Mechanics and Dynamical Astronomy*, Vol. 65, No. 3, 1996, pp. 313–344, doi:10.1007/BF00053511.

[38] E. A. Roth, "The Gaussian Form of the Variation-of-Parameter Equations Formulated in Equinoctial Elements Applications: Airdrag and Radiation Pressure," *Acta Astronautica*, Vol. 12, No. 10, 1985, pp. 719–730, doi:10.1016/0094-5765(85)90088-8.

[39] O. Montenbruck and E. Gill, *Satellite Orbits: Models, Methods and Applications*. X-Pferdchen, Springer-Verlag, 2000.

[40] R. A. Broucke and P. J. Cefola, "On the Equinoctial Orbit Elements," *Celestial Mechanics*, Vol. 5, 1972, pp. 303–310, doi:10.1007/BF01228432.

[41] A. Long, J. Cappellari, C. Velez, and A. Fuchs, "Mathematical Theory of the Goddard Trajectory Determination System," 1976.

[42] M. Rhudy, Y. Gu, J. Gross, and M. Napolitano, "Evaluation of Matrix Square Root Operations for UKF within a UAV GPS/INS Sensor Fusion Application," *International Journal of Navigation and Observation*, Vol. 2011, 2011, pp. 1–11, doi:10.1155/2011/416828.

[43] S. Thrun, W. Burgard, and D. Fox, *Probabilistic Robotics*. The MIT Press, 2005.

[44] S. Holmes, G. Klein, and D. W. Murray, "A Square Root Unscented Kalman Filter for visual monoSLAM," *2008 IEEE International Conference on Robotics and Automation (ICRA)*, 2008, doi:10.1109/ROBOT.2008.4543780.

[45] G. P. Huang, A. I. Mourikis, and S. I. Roumeliotis, "On the Complexity and Consistency of UKF-Based SLAM," *2009 IEEE International Conference on Robotics and Automation*, 2009, doi:10.1109/ROBOT.2009.5152793.

[46] J. K. Miller, A. S. Konopliv, P. G. Antreasian, J. J. Bordi, S. Chesley, C. E. Helfrich, W. M. Owen, T. C. Wang, B. G. Williams, D. K. Yeomans, and D. J. Scheeres, "Determination of Shape, Gravity, and Rotational State of Asteroid 433 Eros," *Icarus*, Vol. 155, No. 1, 2002, doi:10.1006/icar.2001.6753.

[47] A. Konopliv, "A Global Solution for the Gravity Field, Rotation, Landmarks, and Ephemeris of Eros," *Icarus*, Vol. 160, No. 2, 2002, pp. 289–299, doi:10.1006/icar.2002.6975.

[48] H. Schaub and J. L. Junkins, *Analytical Mechanics of Space Systems, Third Edition*. American Institute of Aeronautics and Astronautics, Inc., 2014, doi:10.2514/4.102400.

[49] M. Chernick and S. D'Amico, "New Closed-Form Solutions for Optimal Impulsive Control of Spacecraft Relative Motion," *Journal of Guidance, Control, and Dynamics*, Vol. 41, No. 2, 2017, pp. 301–319, doi:10.2514/1.G002848.

[50] M. Chernick and S. D'Amico, "Closed-Form Optimal Impulsive Control of Spacecraft Formations Using Reachable Set Theory," *AAS/AIAA Astrodynamics Specialist Conference, Snowbird, UT*, 2018.

[51] W. M. Kaula, *Theory of Satellite Geodesy: Applications of Satellites to Geodesy*. Dover Publications, 2000.

[52] J. Giorgini, "JPL Small-Body Database Browser," Accessed: 07.09.2018.

[53] S. Palo, G. Stafford, and A. Hoskins, "An Agile Multi-use Nano Star Camera for Constellation Applications," *AIAA/USU Conference on Small Satellites*, 2013.

[54] P. G. Antreasian, M. Moreau, C. Jackman, K. Williams, B. Page, and J. M. Leonard, "OSIRIS-REx Orbit Determination Covariance Studies at Bennu," *AAS Guidance and Control Conference*, 2016.

[55] "XCAM C3D CubeSat Camera Datasheet," *Northampton, United Kingdom*, 2018.